TPT Trends in Pharmacology and Toxicology

OPEN ACCESS

Structural Consequences of *PRNP* Mutations: An Integrated Docking and Molecular Dynamics Approach to Prion Protein Dysfunction

[1]Kainat Ramzan, [2]Amina Islam and [3]Mobeen Fatima

[1]Department of Biochemistry, Faculty of Life Sciences, University of Okara, Renala Khurd, Okara 56130, Punjab, Pakistan

[2]Department of Microbiology and Molecular Genetics, University of Okara, Renala Khurd, Okara 56130, Punjab, Pakistan

[3]Department of Molecular Biology, University of Okara, Renala Khurd, Okara 56130, Punjab, Pakistan

Corresponding Author: Kainat Ramzan (kainat.ramzan@uo.edu.pk)

ABSTRACT

Background and Objective: Prion protein (PrP), encoded by the *PRNP* gene, is a membrane-associated glycoprotein whose structural integrity is essential for maintaining normal cellular function. Pathogenic mutations in *PRNP* can destabilize the native α-helical conformation of PrP and promote its conversion into a β-sheet-rich misfolded isoform associated with prion diseases. This study aimed to identify deleterious nsSNPs in the *PRNP* gene and assess their impact on prion protein stability and structural integrity. Additionally, potential anti-prion compounds were screened to assess their binding affinity and interaction profiles with both wild-type and mutant PrP, along with an analysis of mutation-induced conformational dynamics. **Materials and Methods:** A total of 43 nsSNPs were prioritized through integrated computational analyses, among which 11 variants were consistently predicted as highly deleterious. The Cys214Tyr and Arg148Cys emerged as the most impactful mutations, showing significant effects on protein stability. Structural modeling revealed a predominantly α-helical C-terminal domain, while binding site prediction identified key pockets overlapping with functionally important and previously reported regions of PrP. **Results:** Molecular docking results demonstrated strong binding affinities of selected compounds, including Flunarizine, Astemizole, Tacrolimus, Amphotericin B, and rifampicin, within these critical regions. These ligands interacted with essential residues such as ARG136, MET134, GLN212, GLU207, ARG208, VAL161, and MET213, indicating their potential role in stabilizing the PrP structure. Molecular dynamics simulations further showed that Arg148Cys and Cys214Tyr mutations significantly destabilize the protein, as evidenced by increased RMSD fluctuations, reduced compactness, and altered energetic profiles. Overall, the findings highlight key structural determinants of PrP stability and suggest that selected compounds may stabilize the prion protein by targeting functionally relevant sites. **Conclusion:** However, these results are based on computational approaches and require experimental validation. Future studies involving in vitro and *in vivo* experiments, extended molecular simulations, and lead optimization are necessary to confirm therapeutic potential and further clarify mechanisms underlying prion protein misfolding and neurodegeneration.

KEYWORDS

Drug repurposing, molecular dynamics simulation, molecular docking, prion diseases, prion protein, *PRNP*, protein stability, structural bioinformatics

ISSN: 2789-9446 (Online)
ISSN: 2789-9438 (Print)
https://doi.org/10.21124/tpt.2026.165.192

Received: 11 May, 2026
Accepted: 22 Aug. 2026
Published: 30 Sep. 2026

INTRODUCTION

Single-nucleotide polymorphisms (SNPs) are the most common form of genetic variation in the human genome, involving single-base-pair substitutions. Around 500,000 SNPs are present within protein-coding regions. Among these, missense mutations (nsSNPs) cause amino acid substitutions that are frequently linked to inherited disorders. These variants can alter protein structure and function by affecting properties such as polarity, hydrophobicity, folding stability, and molecular interactions. Consequently, nsSNPs are major contributors to human disease, and nearly half of genetic disorders are associated with at least one variant-related change[1,2]. Approximately 50-60 well-established pathogenic missense mutations in the *PRNP* gene have been identified as causative factors of inherited prion diseases, including Creutzfeldt-Jakob disease (CJD), fatal familial insomnia (FFI), Gerstmann-Sträussler-Scheinker syndrome (GSS), and Kuru[3].

In the prion protein gene (*PRNP*), several disease-associated mutations have been identified in humans and other mammals. The *PRNP* is located on chromosome 20p13 and encodes the prion protein (PrP), a glycosylphosphatidylinositol (GPI)-anchored membrane glycoprotein comprising an intrinsically disordered N-terminal region and a predominantly α-helical C-terminal domain. Variants such as E200K, D178N, and the M129V polymorphism are key determinants of disease susceptibility and clinical heterogeneity. The E200K mutation is strongly associated with familial CJD, while D178N produces distinct phenotypes depending on the residue at codon 129. The M129V polymorphism acts as a major modifier of disease onset and phenotype. These substitutions destabilize PrP^{C}, increasing its propensity to misfold into the pathogenic PrP^{Sc} isoform, characterized by a transition from α-helical to β-sheet-rich structure and subsequent amyloid aggregation[4-7].

Human susceptibility to prion diseases is further influenced by polymorphisms within the octapeptide repeat (OPR) region. *PRNP* encodes a copper-binding protein implicated in fatal neurodegenerative disorders associated with abnormal prion aggregation. Therapeutic strategies have focused on preventing PrP^{C}-to-PrP^{Sc} conversion and inhibiting aggregate formation; however, once misfolding is initiated, disease progression is largely irreversible, highlighting the importance of early structural stabilization[8]. Structural analyses using nuclear magnetic resonance (NMR) have provided key insights into PrP^{C} conformation, supporting structure-based drug design approaches. Pathological accumulation of PrP^{Sc} in the central nervous system leads to spongiform degeneration and astrogliosis[9,10]. Under physiological conditions, PrP^{C} is widely expressed during development and is primarily localized in neuronal tissues in adults, following the classical secretory pathway involving the endoplasmic reticulum and Golgi apparatus[4,11].

Functionally, PrP^{C} is involved in stress response, myelin maintenance, circadian regulation, mitochondrial function, and metal ion homeostasis, and has roles in neuronal signaling, cell adhesion, and neuroprotection[12]. It interacts with multiple neuronal receptors and contributes to synaptic function. The OPR region binds copper ions and may regulate Cu-Zn superoxide dismutase activity, thereby modulating oxidative stress responses[13]. Genetic variation in *PRNP* has been associated with altered susceptibility to prion diseases in humans and animals. Genome-wide association studies (GWAS) and ClinVar databases further support the role of *PRNP* variants in disease risk and phenotypic variability[14].

This study used an integrated computational strategy to analyze nsSNPs in the PrP Protein. Multiple *in silico* tools were applied to identify deleterious variants and assess their effects on protein stability. In addition, structural modeling and molecular docking were performed to investigate protein-ligand interactions and potential modulators of prion protein activity. Normal Mode Analysis (NMA) was used to evaluate flexibility and conformational changes in both wild-type and mutant proteins. Molecular Dynamics (MD) simulations further examined structural stability and dynamic behavior under physiological conditions. The study aimed to prioritize functionally important nsSNPs linked to altered protein dynamics and neurological disease risk, providing mechanistic insight for future therapeutic development.

MATERIALS AND METHODS

This study employed a computational biology-based approach to identify deleterious variants in the PrP protein and evaluate their effects on protein structure, stability, and ligand-binding properties. The study was conducted during the period from April 2022 to June 2022. A series of bioinformatics tools was applied for variant prediction, functional analysis, structural evaluation, and molecular interaction studies. Selected variants were assessed for their potential impact on protein stability and conformational changes, followed by molecular docking analysis to investigate ligand-binding behavior. The integrated computational workflow ensured reliable and reproducible results, with the complete methodology illustrated in Fig. 1.

Variant assortment from public repositories: The reference nucleotide sequence of the human *PRNP* gene (Gene ID: 5621) was obtained from the National Center for Biotechnology Information (NCBI) database. All reported single-nucleotide polymorphisms (SNPs) associated with the PrP protein were collected from the NCBI dbSNP database (build accessed in 2024) for subsequent comprehensive analysis. The corresponding protein sequence (UniProt ID: P04156) was retrieved from the UniProt Knowledgebase, and the comprehensive list of bioinformatics resources used in this study is provided in Supplementary Table S1.

Functional impact prediction of nsSNPs: The functional impact of coding variants was assessed using multiple sequence- and structure-based tools, including SNPnexus v4, PolyPhen-2, PROVEAN, SNaP, CADD, ConDEL, Align-GVGD, and PredictSNP. SIFT evaluates amino acid substitutions based on evolutionary conservation (scores<0.05 indicate deleterious effects), while PolyPhen/PPh2 classifies variants as benign, possibly damaging, or probably damaging[15,16]. PROVEAN identifies deleterious variants with scores ≤-2.5, and SNaP uses neural networks to distinguish effect from neutral variants. CADD provides a combined deleteriousness score based on diverse genomic features, whereas ConDEL and PredictSNP generate consensus predictions from multiple tools. Variants consistently predicted as damaging were selected for further analysis[17].

Identification of disease-associated nsSNPs: To determine the association between selected nsSNPs and disease phenotypes, additional predictive tools were applied, including PhD-SNP, SNPs&GO, Meta-SNP, and SuSPect. These tools employ machine learning algorithms and evolutionary information to

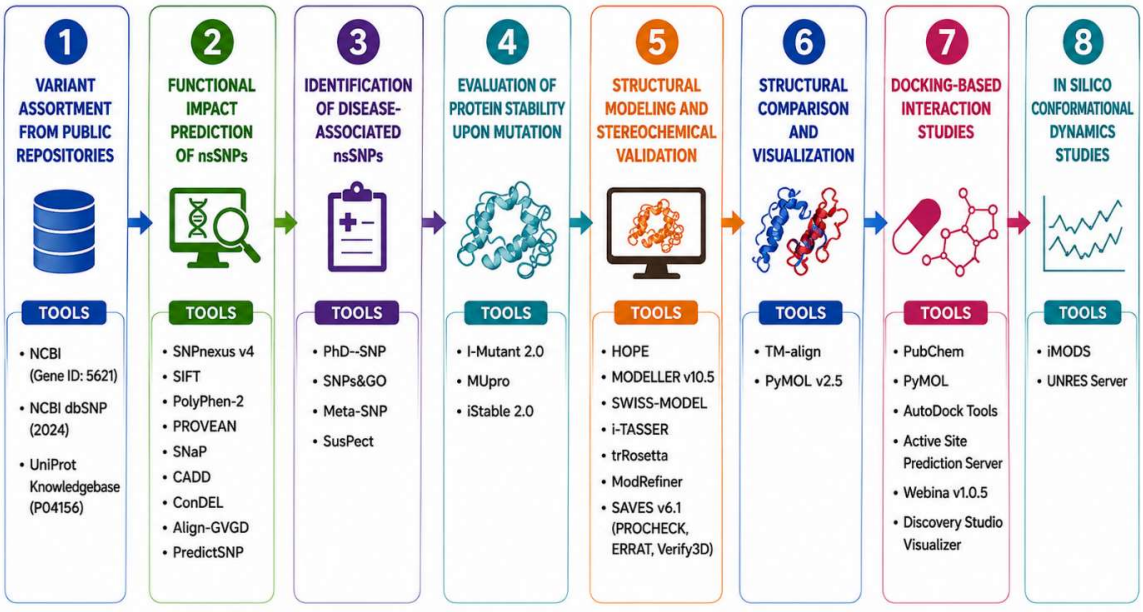

Fig. 1: Computational workflow for analysis of nsSNPs in the human PrP protein

predict whether a mutation is disease-associated. The SNPs&GO incorporates Gene Ontology annotations, while Meta-SNP integrates outputs from multiple predictors to improve overall accuracy. Variants with probability values greater than 0.5 were considered potentially disease-associated effect[18,19].

Evaluation of protein stability upon mutation: The influence of nsSNPs on protein stability was examined using I-Mutant 2.0, MUpro, and iStable 2.0. I-Mutant 3.0 predicts stability changes upon mutation using either sequence- or structure-based information. The analysis was performed at a temperature of 25°C and pH 7.0. MUpro applies machine-learning models to estimate stability changes, where scores below zero indicate decreased stability and scores above zero indicate increased stability. The iStable server 2.0 integrates multiple prediction algorithms to improve the reliability of protein stability assessment following amino acid substitutions[20,21].

Structural modeling and stereochemical validation: Structural effects of selected nsSNPs were examined using the HOPE server by submitting the protein sequence along with specific amino acid substitutions[21]. The analysis assessed variations in residue properties, conservation, and structural context to determine their potential impact on protein stability and function. Three-dimensional structural models of the PrP were generated using multiple computational approaches to ensure model reliability. Homology modeling was performed using MODELLER v10.5, which builds protein structures based on alignment with known template structures. Multiple models were generated, and the best structure was selected based on the lowest DOPE score and molpdf values. Additional structural models were generated using SWISS-MODEL, which identifies suitable templates from the Protein Data Bank and constructs models based on target-template alignment. Protein structure prediction was also performed using i-TASSER, which applies iterative threading and fragment assembly simulations for structure prediction. Furthermore, trRosetta was used to generate models based on predicted inter-residue distance and orientation constraints derived from deep learning methods. The predicted structures were refined using ModRefiner to improve stereochemical quality and overall geometry. Structural validation was performed using SAVES v6.1, which integrates PROCHECK, ERRAT, and Verify3D modules for comprehensive quality assessment. The Ramachandran plot generated by PROCHECK was used to evaluate the stereochemical properties of the models and to determine the percentage of residues located in favored regions[22-24].

Structural comparison and visualization: Structural differences between wild-type and mutant proteins were analyzed using TM-align, which calculates template modeling (TM) scores and root-mean-square deviation (RMSD) values to evaluate structural similarity. Visualization and mutation modeling were performed using PyMOL v2.5, enabling detailed inspection of structural alterations induced by amino acid substitutions[20,25].

Docking-based interaction studies: Ligand structures were obtained from PubChem and converted from SDF to PDB format using PyMOL[26]. The resulting files were then converted into PDBQT format with AutoDock Tools to prepare them for docking. The ligand-binding site of the target protein was predicted using the Active Site Prediction Server, which helped identify the key regions involved in ligand interaction[27]. Docking simulations were performed using Webina v1.0.5, a grid box was defined to encompass the predicted active site, with center coordinates set at x = -47 Å, y = 61 Å, and z = 7 Å, and dimensions of 19 Å×19 Å×19 Å to ensure adequate coverage of the binding pocket. For each ligand, up to 10 binding poses were generated with the exhaustiveness parameter set to 8. The best pose was selected based on the lowest binding energy, along with favorable interactions within the binding site. The docked complexes were analyzed and visualized using Discovery Studio Visualizer to examine protein-ligand interactions and binding orientations[28].

***In silico* conformational dynamics studies:** Normal mode analysis was conducted using the iMODS server to evaluate structural flexibility and possible conformational changes within proteins[29]. Molecular dynamics simulations were performed using the UNRES server at 300 K for 200,000 simulation steps using a Langevin thermostat (friction coefficient = 0.02; coupling constant = 1.0). The simulation length

corresponds approximately to the microsecond (μs) timescale in coarse-grained dynamics, although an exact physical conversion is not strictly defined due to the reduced representation of the UNRES force field. UNRES was selected over all-atom MD platforms (GROMACS or AMBER) because it enables efficient exploration of long-timescale conformational dynamics and global structural rearrangements at significantly reduced computational cost. This makes it particularly suitable for comparative analysis of wild-type and mutant *PRNP* proteins. The resulting trajectories were analyzed using RMSD, radius of gyration, and potential energy to evaluate structural stability and dynamic behavior[30,31].

RESULTS AND DISCUSSION

Screening of functional SNPs: A comprehensive dataset of 14,357 SNPs associated with the human PrP protein was retrieved from the NCBI database along with the corresponding protein sequence for subsequent computational analyses. Among these variants, 816 nsSNPs were located within the coding region of the PrP protein, whereas the remaining variants were distributed across synonymous sites, untranslated regions (5'-UTR and 3'-UTR), and other genomic regions mapped to human chromosome 20 (Fig. 2). Only non-synonymous SNPs were retained for further analysis.

Initially, SIFT predicts 312 deleterious variants and 389 tolerated variants (Fig. 3a). Within the deleterious category, 43 nsSNPs exhibited scores between 0 and 0.04, suggesting a strong likelihood of functional disruption. Notably, 24 variants recorded a score of 0, indicating a high probability of severe structural and functional impairment of the PrP protein (Table S2). Subsequently, PolyPhen scores range from 0 to 1, with values closer to 1 reflecting a higher probability of damaging effects. Based on this analysis, 131 nsSNPs were predicted to be possibly damaging, 260 were classified as benign, and 311 were categorized as probably damaging (Fig. 3b). Furthermore, ten nsSNPs achieved the maximum PolyPhen score of 1.00, highlighting a very high likelihood of structural and functional disruption in the PrP protein (Table S2). Importantly, five variants (Gly127Val, Cys214Tyr, Ser236Phe, Gly29Glu, and Gly127Ser) were consistently predicted as deleterious by both SIFT and PolyPhen, displaying SIFT scores of 0.00 and PolyPhen scores of 1, indicating strong evolutionary conservation and potential functional significance. Based on the PolyPhen 2, a subset of 43 nsSNPs was identified as highly deleterious, with PolyPhen scores ranging from 0.911 to 1.00. The SNaP evaluates the functional impact of amino acid substitutions using a scoring range

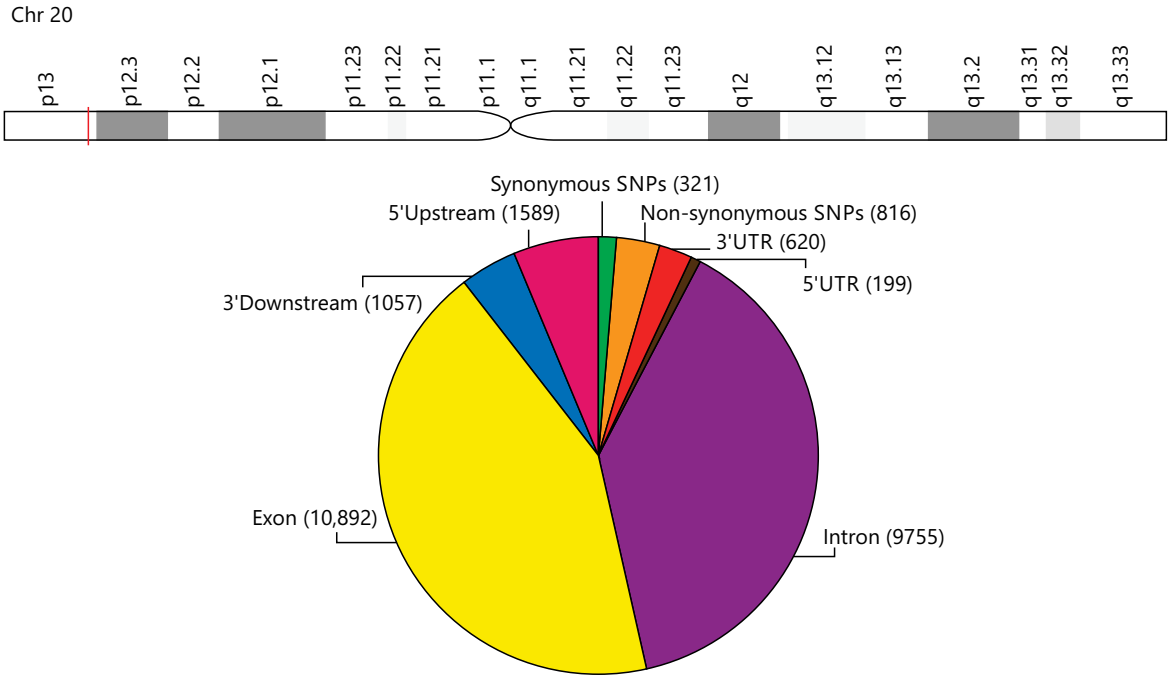

Fig. 2: A graphical depiction of the SNP prevalence in the PrP protein, which is located on chromosome 20

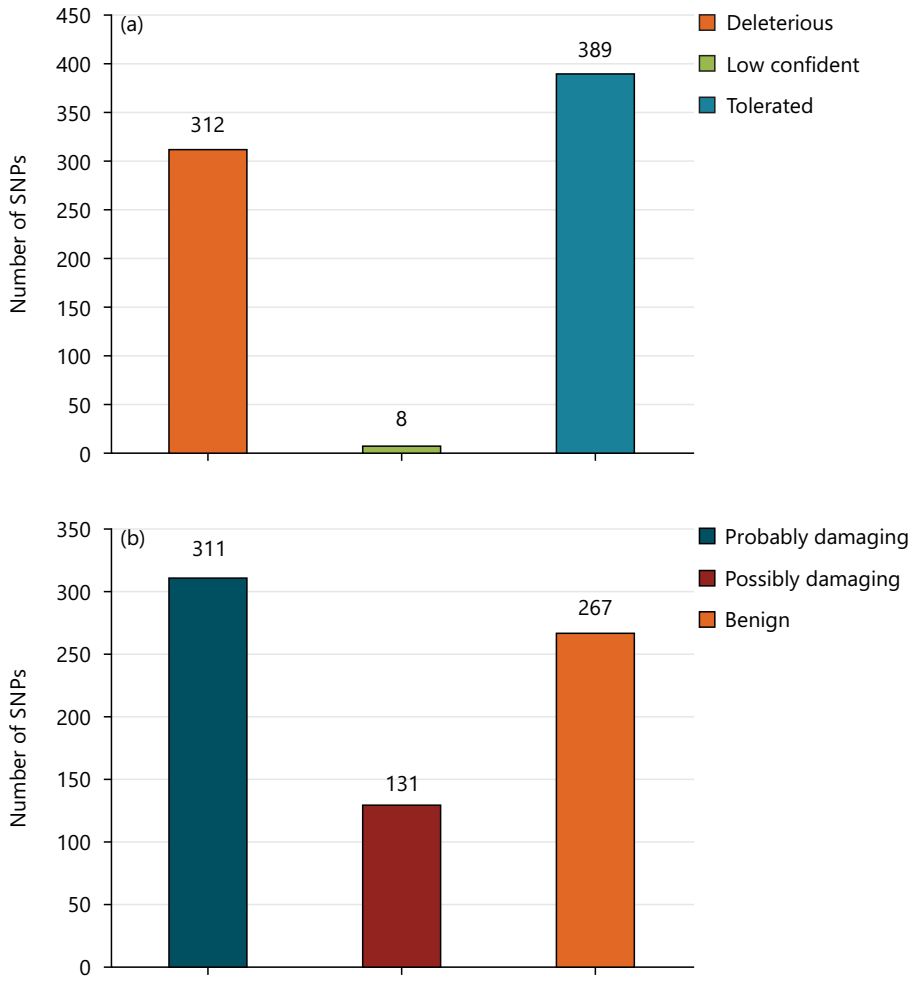

Fig. 3(a-b): Prediction of deleterious SNPs from the (a) SIFT and (b) PolyPhen servers

SNPs, Single nucleotide polymorphisms and SIFT: Sorting intolerant from tolerant, a computational tool used to predict the functional impact of amino acid substitutions

from -100 to +100, where positive scores indicate a higher probability of functional effects. The analysis predicted that 40 nsSNPs are likely to affect PrP function, whereas Val122Gly, Ser236Thr, and Thr188Met were predicted to be functionally neutral. Moreover, PROVEAN analysis classified 11 nsSNPs as deleterious and 32 variants as neutral. However, Pro76Arg, Cys214Tyr, and Pro50Leu showed the strongest functional impact with PROVEAN scores of -3.91, -3.76, and -3.48, respectively, indicating a high probability of deleterious effects (Table S2).

Further structural and evolutionary evaluation using the Align-GVGD algorithm categorized the 43 nsSNPs into several functional classes, including C65 (n = 27), C55 (n = 6), C45 (n = 1), C25 (n = 3), and C15 (n = 2). Variants assigned to classes C45, C55, and C65 are generally associated with significant functional consequences, whereas classes C0, C15, C25, and the intermediate class C35 typically represent variants with minimal or no functional impact. Based on this classification, variants such as rs1313855686, rs761807915, rs1197612803, rs1323478206, rs74315403, rs74315413, and rs74315414 were predicted to have no substantial functional effect on the *PRNP* protein. Finally, the PredictSNP consensus predictor further supported these findings by classifying Val122Gly as a functionally neutral variant. Based on the combined results of SIFT and PolyPhen, the 43 highly deleterious nsSNPs were selected for subsequent structural and functional analyses (Table S2). The study found that 11 nsSNPs (Gly127Val, Cys214Tyr, Pro50Leu, Pro76Arg, Pro102Leu, Pro105Leu, Gly131Val, His187Arg, Arg148Cys, Gly29Glu, and Gly58Trp)

Table 1: Integrated prediction of deleterious *PRNP* nsSNPs based on functional, disease association, and stability analyses

SNVs	Functional analysis (9 Tools)	Disease annotation (5 Tools)	Protein stability (3 Tools)
rs267606980	Gly127Val	Gly127Val	-
rs1180897417	Cys214Tyr	Cys214Tyr	Cys214Tyr
rs1379757697	Pro50Leu	-	-
rs778667313	Pro76Arg	-	-
rs74315401	Pro102Leu	-	-
rs11538758	Pro105Leu	-	-
rs74315410	Gly131Val	Gly131Val	-
rs74315413	His187Arg	-	-
rs750548556	Arg148Cys	Arg148Cys	Arg148Cys
rs989264799	Gly29Glu	-	-
rs773938628	Gly58Trp	Gly58Trp	-

were consistently predicted as highly deleterious across all applied *in silico* prediction tools, suggesting that these variants may play a critical role in altering the structural stability and functional properties of the protein (Table 1).

Evaluation of disease association of nsSNPs: A total of 43 nsSNPs in the PrP protein were evaluated using SuSPect, SNP&GO, PhD-SNP, and Meta-SNP to assess their disease association. SuSPect classified most variants as disease-causing, whereas a few were predicted as neutral. Similarly, PhD-SNP analysis indicated that most variants were disease-associated, while 10 nsSNPs were classified as neutral, and the remaining were predicted to be disease-causing. SuSPect predicted several variants, including Gly195Arg, Lys24Arg, Gly92Glu, Glu200Lys, Arg37Gln, and Gly29Glu, to have a neutral effect on the PrP protein. In addition, Meta-SNP analysis identified 17 nsSNPs as neutral, while the remaining variants were predicted to be disease-causing (Table S3). However, Gly127Val, Cys214Tyr, Gly131Val, Arg148Cys, and Gly58Trp were consistently predicted as disease-causing across all computational tools (Table 1).

Analysis of protein stability: The impact of nsSNPs on PrP stability was evaluated using MuPro, I-Mutant 2.0, and iStable 2.0 (Table S4). According to MuPro, most variants were predicted to decrease protein stability; however, Gly127Val, Ser236Phe, and Gly131Val were found to increase stability. The I-Mutant 2.0 results showed that the majority of substitutions exhibited negative ΔΔG values, indicating a reduction in protein stability, while a limited number of variants showed slight stabilizing effects based on RI values. Similarly, iStable 2.0 indicated that 11 nsSNPs were identified as stabilizing mutations, whereas 32 nsSNPs were associated with decreased protein stability, suggesting that the majority of variants may adversely affect PrP protein structural integrity and function (Table S4). Finally, Cys214Tyr and Arg148Cys were consistently predicted as highly deleterious by all 17 computational tools (Table 1); therefore, these mutations were selected for further docking analysis.

Structural effect of nsSNPs: The HOPE analysis indicated that the Cys214Tyr mutation replaces cysteine with a larger tyrosine residue, which may not properly fit in the local structural environment. The difference in hydrophobicity between the wild-type and mutant residues can lead to the loss of hydrophobic interactions within the protein core, potentially disturbing the stability of the protein structure. In contrast, the Arg148Cys mutation substitutes arginine with cysteine, resulting in a smaller residue and the loss of the positive charge present in the wild-type amino acid. This change may reduce ionic interactions and external contacts with surrounding residues or molecules, which can weaken local structural stability and affect normal protein interactions (Fig. 4).

Comparative modeling and validation: The comparative validation results presented in Table 2 demonstrate that P40258.1.A, generated using the SWISS-MODEL server, displayed the overall structural quality among all evaluated models (Fig. 5a). The model was further refined using ModRefiner, and its QMEAN4 score was -5.95 (Fig. 5b). This model achieved the highest ERRAT score of 98.57, indicating

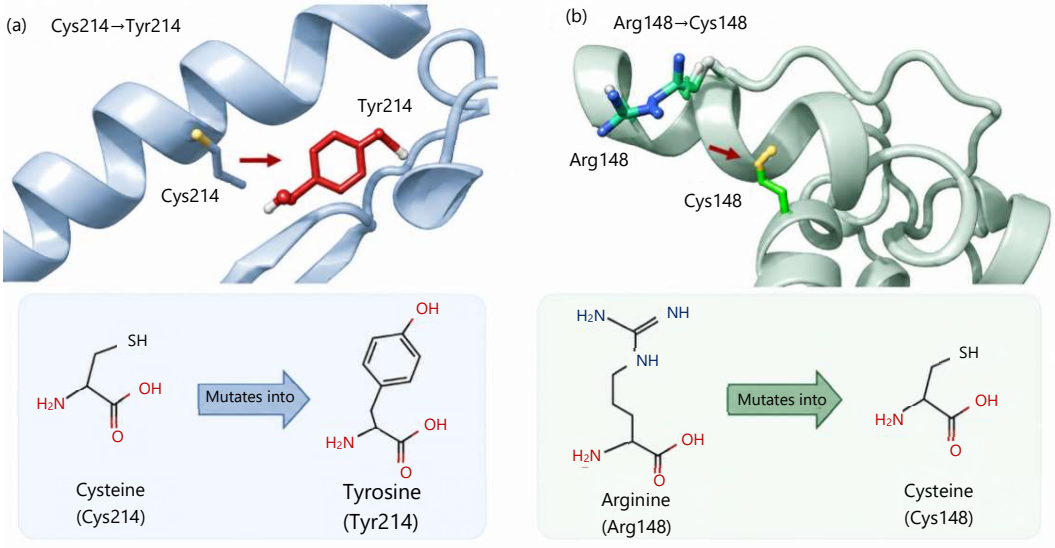

Fig. 4: Structural representation of missense mutations in the PrP protein

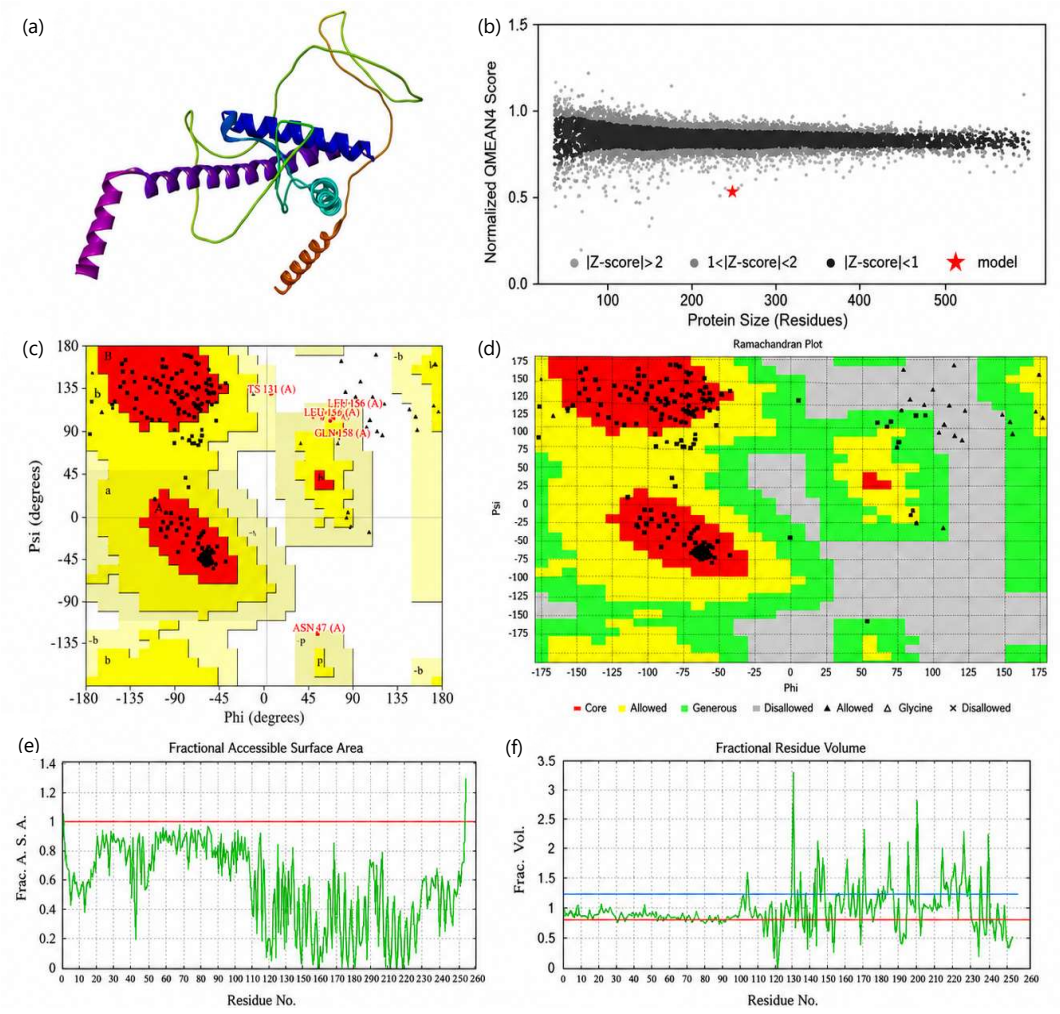

Fig. 5(a-f): Structural validation and physicochemical analysis of the modeled PrP structure, (a) 3D structure of the predicted prion protein (PrP) model, (b) QMEAN quality estimation plot for model reliability assessment, (c) PROCHECK Ramachandran plot showing backbone dihedral angle distribution, (d) VADAR analysis of structural properties, (e) Fractional accessible surface area (ASA) profile of residues and (f) Fractional residue contribution/value analysis highlighting residue-level structural features

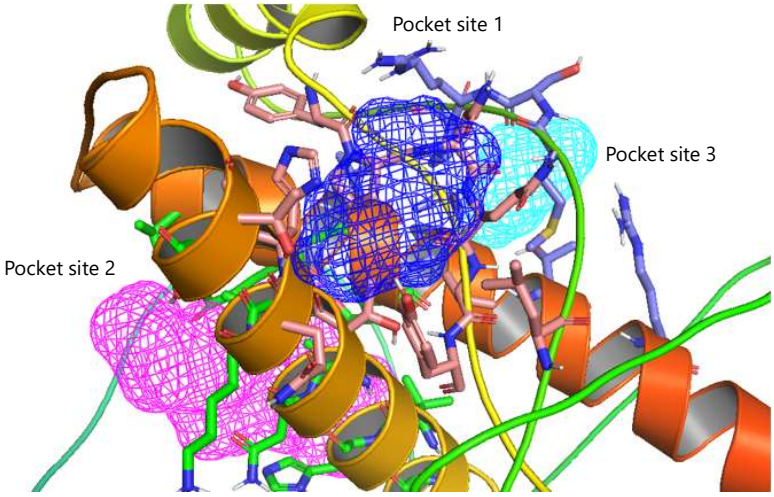

Fig. 6: Predicted binding sites of prion protein (PrP) identified by active site analysis

Table 2: Comparative validation analysis of PrP protein structural models using SAVES v6.1 assessments

Validation parameter	TRmodel5	prp.B99990006	P40258.1.A	i-TASSER (Model 01)
ERRAT score	87.76	10.26	98.57	20.31
Verify3D (%)	58.10	67.59	66.01	64.03
Most favored (%)	80.5	72.1	88.9	75.80
Allowed (%)	16.3	19.5	6.8	14.20
Generously allowed (%)	0.0	4.7	4.2	6.30
Disallowed (%)	3.2	3.7	0.0	3.70

strong structural reliability. Its Verify3D score of 66.01% further confirmed good compatibility of residues in the 3D-1D profile. PROCHECK analysis also supported its quality, with 88.9% residues in most favored regions and no residues in disallowed regions (Fig. 5c). The PrP protein was further analyzed using the VADAR server to evaluate its structural features (Fig. 5d).

The results showed that the protein is mainly α-helical, containing 41% α-helices, 6% β-sheets, and 51% coil regions. Turn regions accounted for 11% of residues, indicating the presence of flexible loop segments connecting secondary structural elements. Hydrogen bond analysis showed an average bond distance of 2.2 Å and a mean energy of -1.9 kcal/moL. Slightly more than half of the residues were involved in hydrogen bonding, suggesting that several regions of the protein are exposed to solvent rather than being tightly packed in the core. Backbone dihedral angles were within the expected range for α-helical structures, while side-chain conformations largely followed standard stereochemical preferences, with only a small number of residues adopting cis configurations. Surface area analysis revealed a total solvent-accessible surface area of 23,722 $Å^2$, with a higher proportion of polar residues compared to charged residues, indicating good solubility and interaction potential. Volume analysis further confirmed moderate packing consistent with a folded protein of approximately 27.7 kDa. Fractional accessible surface area (ASA) profile of residues (Fig. 5e), and fractional residue contribution/value analysis highlighting residue-level structural featuresa (Fig. 5f). Overall, the PrP protein exhibits a helix-rich, moderately packed, and solvent-accessible structure with flexible loop regions, supporting its structural stability and functional behavior.

Binding site prediction: The Active Site Prediction server predicted three binding pockets in the protein, which were visualized using PyMOL (Fig. 6). In each structure, Pocket 1 is located at the interface of two structural regions, Pocket 2 is present within a core secondary structure region, while Pocket 3 is found at a surface-exposed loop/helix junction. The first binding site (Site 1) includes residues Leu130, Tyr157, Pro158, Asn159, Gln160, Val161, Tyr162, Thr183, Gln186, His187, and Thr190. The second site (Site 2) consists of Asn173, Val176, His177, Val180, Asn181, Ile184, Lys185, Thr188, Val203, Glu207, and Arg208.

Table 3: ADMET and drug-likeness profiling of anti-prion/anti-aggregation compounds using SWISSADME

Compound	Prediction	PAINS alerts	Brenk alerts	Lead-likeness	Synthetic accessibility	Bioavailability Score	P-gp substrate	CYP1A2 inhibitor	CYP2C19 inhibitor	CYP2C9 inhibitor	CYP2D6 inhibitor	CYP3A4 inhibitor	Skin permeation (Log Kp, cm/s)
Quinacrine	Inactive	1	1	No	3.19	0.55	Yes	Yes	No	No	Yes	Yes	-4.46
Pentosan polysulfate	Inactive	0	1	No	5.88	0.11	Yes	No	No	No	No	No	-13.94
Chlorpromazine	Active	0	0	No	3.12	0.55	No	Yes	Yes	Yes	Yes	No	-4.56
Emrusolmin	Active	0	0	No	2.77	0.55	Yes	Yes	Yes	Yes	Yes	Yes	-5.52
Amphotericin B	Moderate	0	0	No	10	0.17	Yes	No	No	No	No	No	-14.06
Suramin	Inactive	0	1	No	6.41	0.11	Yes	No	No	No	No	No	-13.12
Rapamycin	Inactive	0	2	No	10	0.17	Yes	No	No	No	No	No	-7.6
Minocycline	Moderate	0	1	No	4.68	0.11	Yes	No	No	No	No	No	-7.56
Guanabenz	Moderate	0	2	No	2.3	0.55	No	Yes	No	No	No	No	-6.48
Flunarizine	Active	0	0	No	3.11	0.55	Yes	No	No	No	Yes	No	-4.66
Tacrolimus	Moderate	0	2	No	9.72	0.17	Yes	No	No	No	No	Yes	7.88
Celecoxib	Active	0	0	No	2.74	0.55	No	Yes	No	Yes	No	No	-6.21
Rifampicin	Active	0	0	No	2.46	0.11	No	No	No	No	No	Yes	-6.48
Astemizole	Active	0	0	No	3.31	0.55	Yes	No	Yes	No	Yes	Yes	-4.86
Promethazine	Inactive	1	0	No	3.54	0.55	No	Yes	No	Yes	Yes	No	-4.62
Congo Red	Inactive	1	3	No	4.22	0.17	Yes	No	No	No	No	No	-6.48
Curcumin	Moderate	0	2	No	2.97	0.55	No	No	No	Yes	No	Yes	-6.28
Trehalose	Active	0	0	Yes	5.22	0.17	Yes	No	No	No	No	Yes	-11.36
Flupirtine	Active	0	0	Yes	2.72	0.55	Yes	Yes	No	No	Yes	No	-6.48
Simvastatin	Active	0	1	No	5.8	0.55	No	No	No	Yes	No	Yes	-5.53

The third site (Site 3) is formed by Met134, Ser135, Arg136, Pro137, Val209, Gln212, Met213, Thr216, and Arg220. Several of these residues, especially histidine, lysine, arginine, glutamine, and glutamic acid, are known to play important roles in neurological function and ligand interactions. These amino acids are commonly involved in protein binding, receptor modulation, and stabilization of protein structures in neuro-related systems.

In PrP, previous studies have reported key functional regions that are important for therapeutic targeting. The hydrophobic core region (residues 112-133) is strongly associated with protein misfolding and aggregation. The C-terminal helical region (residues 160-230), including Helix 2 (172-194) and Helix 3 (200-230), is important for structural stability. Residues such as His187, Lys185, Tyr162, Arg208, and Met213 are reported to contribute to folding stability and functional regulation. In addition, the disulfide bond between Cys179 and Cys214 plays a critical role in maintaining structural integrity[32-34]. Comparison of predicted binding sites with reported functional regions shows that residues such as His187, Lys185, Arg208, and Met213 are present in the identified pockets. These residues are therefore considered potential therapeutic targets for ligand binding and stabilization, which may help in controlling PRP misfolding and related neurodegenerative processes.

ADME properties: A library of 20 compounds, comprising approved drugs, withdrawn agents, and experimentally reported anti-prion/anti-aggregation molecules, was screened to evaluate their potential for inhibiting PrP protein misfolding and aggregation. The pharmacokinetic and drug-likeness profiles were assessed using the SWISSADME platform, revealing considerable variability among the compounds (Table 3). The predicted bioavailability scores ranged from 0.11 to 0.55, indicating moderate to low oral drug-likeness for most molecules. Several compounds, including pentosan polysulfate, suramin, rapamycin, amphotericin B, and minocycline, showed poor predicted oral bioavailability, likely due to their high molecular weight and polar surface area. PAINS and Brenk filter analyses indicated generally acceptable chemical safety profiles across the dataset, although quinacrine, promethazine, and Congo red exhibited structural alerts suggesting potential chemical liabilities. Lead-likeness evaluation revealed that only trehalose and flupirtine met strict lead-like criteria, whereas the remaining compounds fell outside the conventional lead-like chemical space due to greater molecular complexity. Synthetic accessibility scores varied widely, with relatively simpler molecules such as guanabenz and flupirtine predicted to be more synthetically feasible. In contrast, structurally complex compounds including rapamycin, tacrolimus, and amphotericin B were associated with higher synthetic difficulty.

P-glycoprotein substrate predictions suggested that a substantial proportion of the compounds may be susceptible to efflux transport, potentially limiting central nervous system (CNS) penetration. However, compounds such as chlorpromazine, emrusolmin, flunarizine, astemizole, and quinacrine displayed variable transporter interactions that may influence their bioavailability in neural tissues. Cytochrome P450 inhibition profiling indicated frequent inhibition of key isoforms (CYP3A4, CYP2D6, and CYP1A2), particularly by chlorpromazine, emrusolmin, astemizole, and simvastatin, highlighting a potential risk of drug-drug interactions. In contrast, compounds such as minocycline and suramin exhibited minimal predicted CYP inhibition. Skin permeability (log Kp) analysis showed generally low dermal absorption for highly polar compounds such as pentosan polysulfate, trehalose, and suramin, whereas moderately lipophilic compounds, including quinacrine, flunarizine, and chlorpromazine, demonstrated comparatively higher permeability. Notably, tacrolimus exhibited a relatively higher positive log Kp value, suggesting enhanced membrane permeability compared with most other compounds. Based on biological activity screening, only compounds predicted as "active" or "moderately active" were selected for subsequent molecular docking studies to focus on the most promising anti-prion candidates (Table 4).

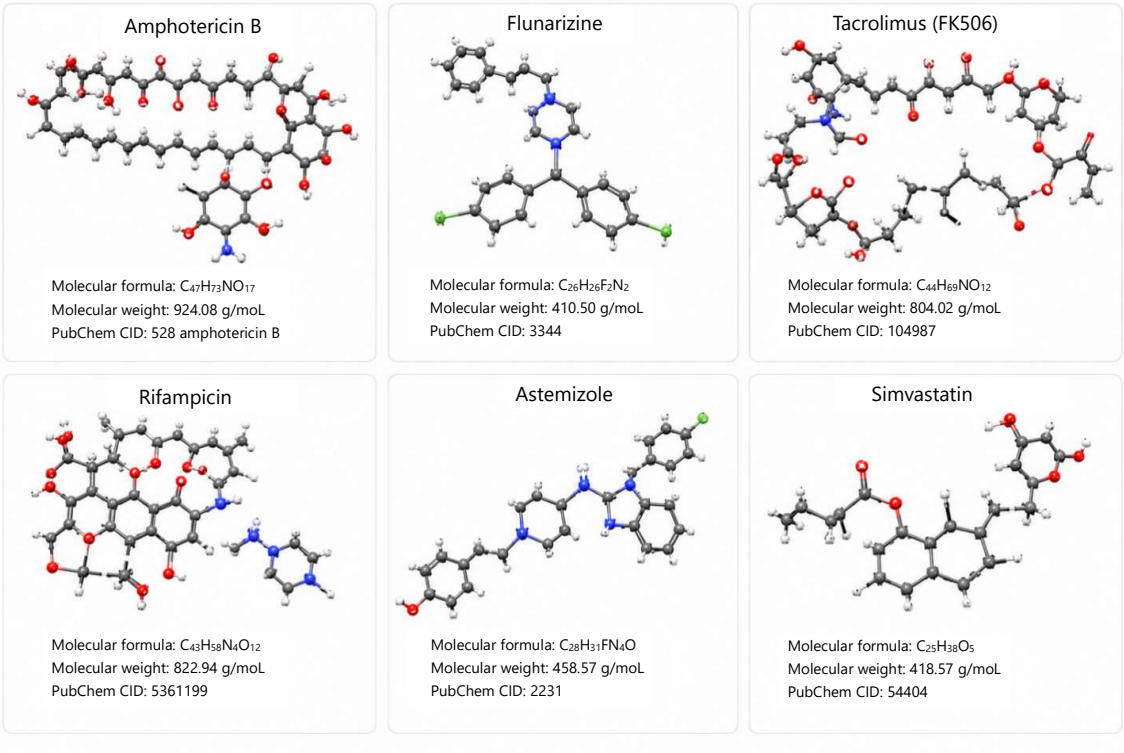

Fig. 7: 3D structures of top selected compounds used for molecular docking against PrP

Table 4: Physicochemical and structural properties of selected anti-prion/anti-aggregation compounds

Compound	Molecular weight (Da)	LogP	HBA	HBD	TPSA (Å^2)	Rotatable Bonds	PubChem CID
Chlorpromazine	318.9	5.2	3	0	31.8	4	2726
Emrusolmin (Anle138b)	~347	4.2	3	1	44	4	445607
Amphotericin B	924.1	0.8	18	12	319	6	14956
Minocycline	457.5	0.6	9	5	151	4	54675776
Guanabenz	231.7	2.7	3	2	55	3	3516
Flunarizine	404.5	5.6	2	0	12	6	941361
Tacrolimus (FK506)	804	3.3	11	3	178	10	445643
Celecoxib	381.4	3.5	3	1	86	4	2662
Rifampicin	822.9	3.7	16	6	220	7	5381226
Astemizole	458.6	6.7	4	0	38	8	2237
Curcumin	368.4	3.2	6	2	93	8	969516
Trehalose	342.3	-3.7	11	8	190	4	7427
Flupirtine	304.3	2.1	4	2	70	5	3394
Simvastatin	418.6	4.7	5	1	72	7	54454

Virtual screening of compounds: Molecular docking analysis was performed using Webina 1.0.5 to investigate the binding interactions of selected anti-prion compounds with the wild-type PrP and its two mutant variants (Cys214Tyr and Arg148Cys). The 3D structures of the selected compounds (Fig. 7). Against the wild-type PrP, the strongest binding affinities were observed for astemizole (-9.874 kcal/moL), flunarizine (-9.256 kcal/moL), and simvastatin (-9.068 kcal/moL), indicating their strong interaction potential with the native protein structure. For the Cys214Tyr mutant, a general decrease in binding affinity was observed for most compounds. However, tacrolimus exhibited the highest binding affinity (-9.133 kcal/moL), followed by flunarizine (-7.32 kcal/moL) and rifampicin (-7.258 kcal/moL), suggesting relatively stable interactions despite the mutation. In the case of the Arg148Cys mutant, amphotericin B showed the strongest binding affinity (-8.972 kcal/moL), followed by tacrolimus (-8.553 kcal/moL) and astemizole (-7.745 kcal/moL). These findings indicate that certain ligands maintain favorable binding interactions even in the presence of structural variations in the prion protein (Table 5).

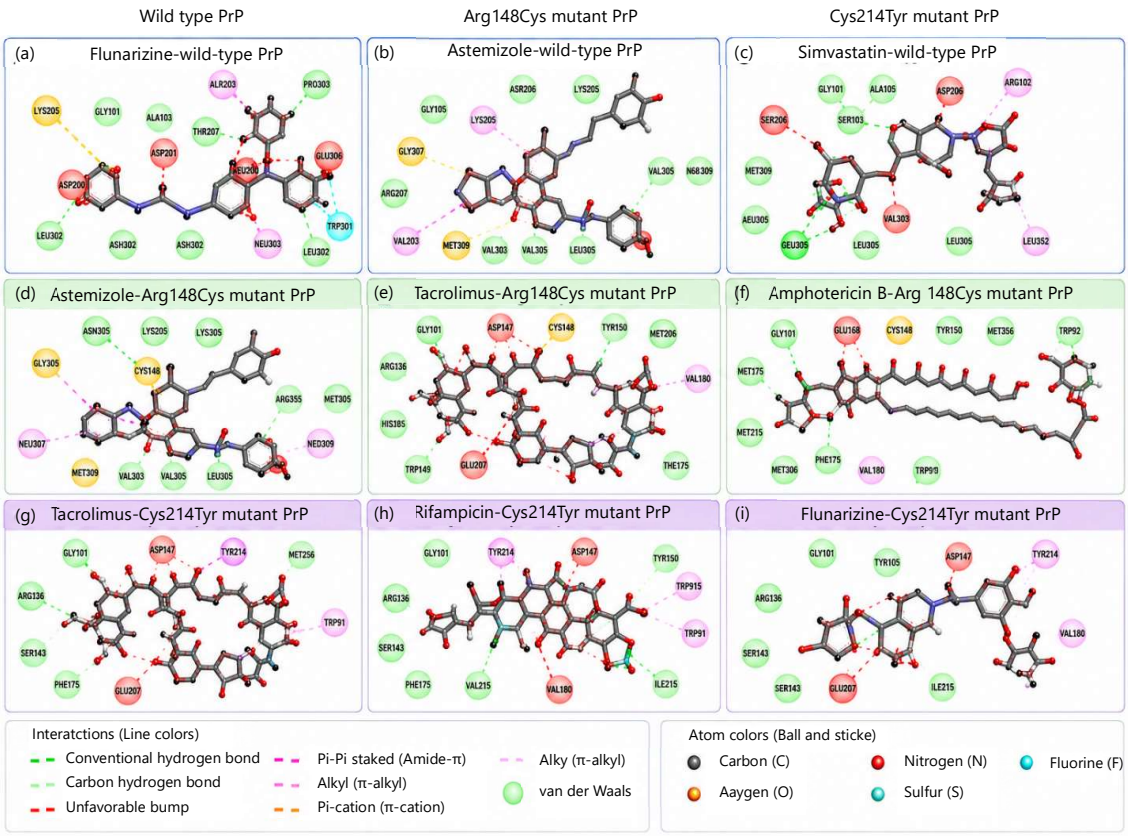

Fig. 8(a-i): Molecular interaction profiles of selected compounds with prion protein (PrP), (a-c) Flunarizine, Astemizole, and Simvastatin bound to wild-type PrP, (d-f) Astemizole, Tacrolimus, and Amphotericin B interacting with the Arg148Cys mutant and (g-i) Tacrolimus, Rifampicin, and Flunarizine bound to the Cys214Tyr mutant, illustrating comparative binding modes across wild-type and mutant PrP structures

Table 5: Molecular docking binding affinities (-kcal/moL) of selected anti-prion compounds

Compound name	Wild type	Cys214Tyr	Arg148Cys
Chlorpromazine	-7.184	-5.526	-5.78
Emrusolmin	-8.582	-7.071	-7.238
Amphotericin B	-8.453	-6.094	-8.972
Minocycline	-8.44	-6.257	-6.958
Guanabenz	-7.607	-5.278	-4.796
Flunarizine	-9.256	-7.32	-6.967
Tacrolimus (FK506)	-8.251	-9.133	-8.553
Celecoxib	-8.256	-7.133	-7.442
Rifampicin	-7.071	-7.258	-5.776
Astemizole	-9.874	-6.824	-7.745
Curcumin	-5.286	-5.002	-4.463
Trehalose	-4.288	-5.581	-6.32
Flupirtine	-6.706	-6.043	-5.447
Simvastatin	-9.068	-7.036	-5.847

Protein-ligand interaction profiling of the selected compounds was performed using Discovery Studio Visualizer following molecular docking with Webina 1.0.5 (Fig. 8a-i). The interactions were analyzed in terms of hydrogen bonds, hydrophobic contacts, π-interactions, halogen bonding, and unfavorable steric contacts to evaluate binding stability across wild-type PrP and its mutant variants (Table S5). In the wild-type PrP, flunarizine exhibited a broad interaction network including a π-cation interaction with ARG136, π-sulfur interaction with MET154, alkyl interaction with ILE215, halogen bonding with THR216, and extensive van der Waals contacts with residues such as PHE175, TYR163, GLN212, and TYR157. However, several unfavorable bump interactions were also observed around GLN212, MET213, and

CYS214, indicating steric constraints within the binding pocket. Astemizole showed stabilization through π-sulfur interactions (MET134, CYS179), π-alkyl interaction (VAL176), and a wide range of van der Waals contacts, although unfavorable interactions were detected with GLN160, GLU211, and GLN212. Simvastatin formed a conventional hydrogen bond with GLN212 along with alkyl interactions (MET134, VAL209) and extensive hydrophobic contacts, but also displayed unfavorable interactions near ARG136 and CYS214.

In the Arg148Cys mutant, astemizole maintained strong binding interactions, including a conventional hydrogen bond with GLN212, π-π stacking with PHE175, π-sulfur interaction with MET213, halogen bonding with VAL209, and alkyl interactions with ILE139 and PHE141. Tacrolimus formed hydrogen bonds with GLU207 and MET206, carbon-hydrogen interactions with ARG206 and GLU176, and π-alkyl contacts with VAL180 and ILE215, although unfavorable donor-donor and steric clashes were also observed. Amphotericin B showed a key hydrogen bond with ASP148 and hydrophobic interactions with VAL180 and ILE179, supported by extensive van der Waals contacts throughout the binding pocket. For the Cys214Tyr mutant, flunarizine displayed halogen interactions and π–alkyl contacts, but also showed multiple unfavorable bump interactions around ARG214 and neighboring residues. Rifampicin formed hydrogen bonds with GLU207, ASP178, and VAL161, along with π-π stacking with ARG136, although steric clashes were also observed within the binding region. Tacrolimus demonstrated hydrogen bonding with GLN212, carbon-hydrogen bonding with ARG208 and GLU211, and π-alkyl interactions with TRP81 and VAL180, but also showed unfavorable interactions, particularly around GLU211. However, astemizole, flunarizine, tacrolimus, rifampicin, and amphotericin B exhibited the most diverse and stable interaction profiles across wild-type and mutant proteins. The presence of hydrogen bonding, hydrophobic contacts, and π-interactions supports their strong binding potential, while observed unfavorable steric clashes highlight the structural constraints introduced by mutations in the prion protein.

All interacting residues of PrP protein identified in this study, including ARG136, HIS140, PHE141, ASP147, ARG148, TYR150, TYR157, HIS155, TYR162, TYR163, ARG164, ASP178, CYS179, VAL180, ILE182, THR183, MET134, SER135, PRO137, ILE138, ILE139, GLN160, VAL161, VAL176, VAL209, VAL210, GLU211, GLN212, MET213, CYS214, ILE215, THR216, GLN217, TYR218, and CYS219, have been previously described in the literature as structurally and functionally important residues involved in ligand binding and PrP stability. The docking analysis further indicates that the selected compounds interact with residues that show strong overlap with FT Site-predicted binding pockets and literature-supported functional regions. In particular, residues such as ARG136, MET134, GLN212, GLU207, ARG208, VAL161, and MET213 were consistently involved in ligand interactions across different protein variants, highlighting their importance in binding stability and prion misfolding processes. Overall, these findings confirm that ligand binding occurs at biologically relevant sites, supporting the potential of the selected compounds as promising anti-prion candidates. Additionally, residues reported in literature and identified through FT Site analysis were highlighted in bold within the interaction table to clearly distinguish key functional binding-site residues from other contacts (Table S5). These include ARG136, MET134, GLN212, GLU207, ARG208, VAL161, MET213, VAL176, VAL180, and CYS214, which are critically involved in maintaining PrP structural integrity and misfolding regulation.

Normal mode analysis (NMA): The NMA was performed using the iMODS server to assess the structural dynamics of the PrP protein and its variants. This analysis produced deformability plots, B-factor mobility profiles, and eigenvalue distributions, which together provide insight into the flexibility and stability of the protein structures. The PrP protein showed an eigenvalue of 1.393523×10^{-8}, indicating a relatively flexible structure that requires lower energy for conformational change. The deformability profile displayed several peaks along the residue positions, suggesting that flexibility is mainly present in loop and surface regions. The B-factor plot also showed moderate fluctuations throughout the protein chain, reflecting normal residue mobility within the native conformation (Fig. 9a). In the Arg148Cys mutant, the eigenvalue increased to 1.116813×10^{-6}, indicating greater structural rigidity compared with the wild type. The

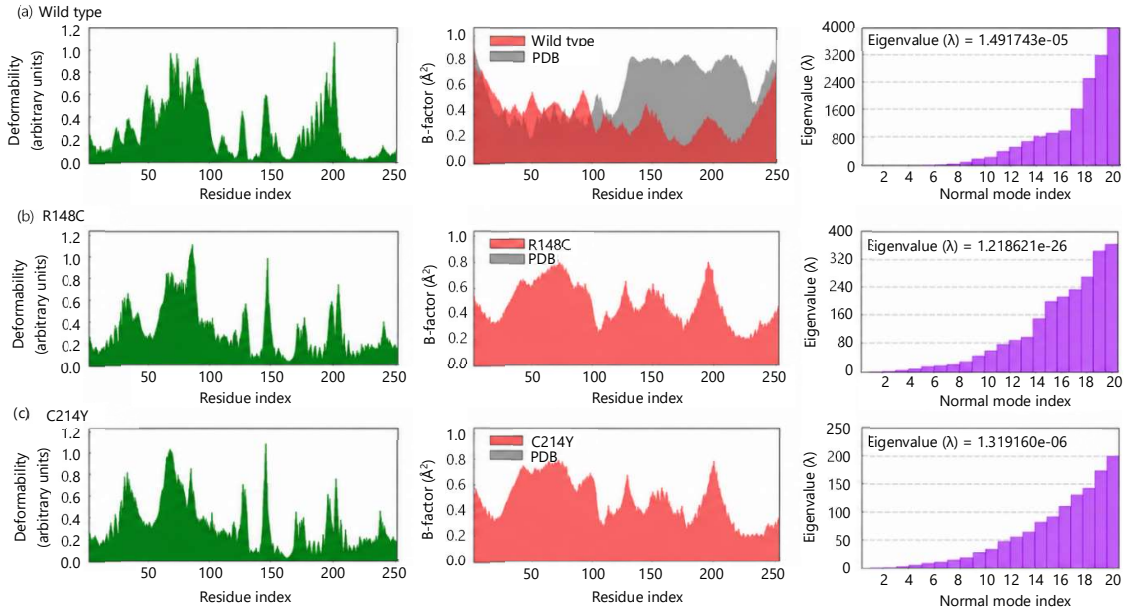

Fig. 9(a-c): (a) NMA profiles of wild-type PrP showing residue deformability, B-factor mobility, and eigenvalue distribution, reflecting the intrinsic flexibility and dynamic behavior of the native protein, (b) NMA profiles of the R148C mutant displaying residue deformability, B-factor mobility, and eigenvalue distribution, indicating altered dynamic properties relative to the wild-type protein and (c) NMA profiles of the C214Y mutant showing residue deformability, B-factor mobility, and eigenvalue distribution, suggesting mutation-associated changes in protein flexibility and motion

deformability plot revealed localized peaks at certain residues, showing limited but noticeable flexibility in specific regions. The B-factor profile showed variation along the sequence but followed a pattern similar to that of the wild-type structure (Fig. 9b). The Cys214Tyr mutant showed an eigenvalue of 1.389190×10^{-6}, which is also higher than that of the wild type. This increase suggests a more rigid structure with reduced overall mobility. The deformability analysis highlighted several flexible regions, while the B-factor profile indicated moderate residue movement across the protein (Fig. 9c). The significant increase in eigenvalues for the Arg148Cys and Cys214Tyr mutants indicates that these mutations cause greater structural stiffness, which suggests an alteration in the dynamic behavior and conformational flexibility of the prion protein.

Molecular dynamics (MD) simulations: The MD simulations revealed notable differences in stability and conformational behavior between wild-type (WT) and mutant prion proteins based on comparative analysis of potential energy, backbone root-mean-square deviation (RMSD), and radius of gyration (Fig. 10a-c). The PrP protein exhibited a rapid decrease in potential energy during the initial equilibration phase, followed by convergence to a stable plateau, indicating attainment of an energetically favorable and equilibrated state. In contrast, both mutants showed a continuous decline in potential energy throughout the simulation period, without clear convergence. This behavior suggests incomplete equilibration and reduced thermodynamic stability in the mutant systems. The WT protein reached a stable RMSD plateau after an initial equilibration period, indicating convergence to a stable conformational state. Conversely, both Arg148Cys and Cys214Tyr variants displayed higher RMSD values with persistent fluctuations over time, reflecting ongoing conformational rearrangements and a lack of structural stabilization. Among the mutants, Cys214Tyr showed comparatively greater deviation, suggesting stronger destabilization. However, analysis of the radius of gyration demonstrated that the WT PrP maintained a consistently low and stable Rg value throughout the simulation, indicative of a compact and well-folded structure. In contrast, both mutants exhibited higher and more fluctuating Rg values, suggesting reduced compactness, increased structural flexibility, and partial unfolding tendencies.

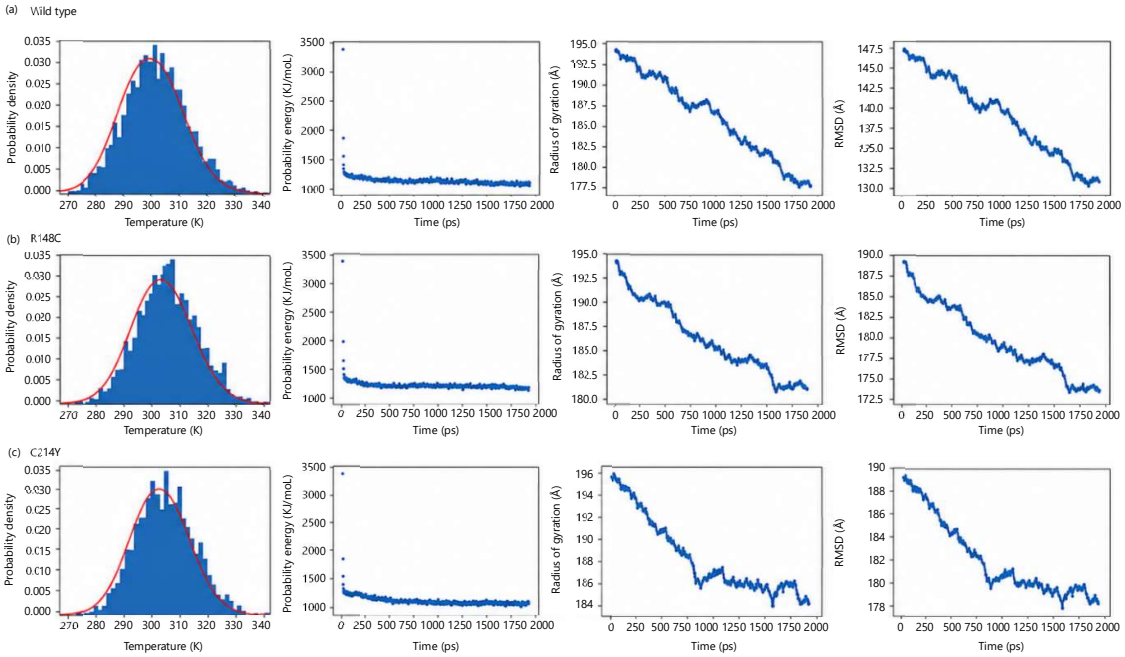

Fig. 10(a-c): MD simulation profiles of the (a) MD simulation profiles of wild-type PrP showing stable temperature equilibration (~300 K), potential energy stabilization, and relatively stable Rg and RMSD trajectories throughout the simulation, (b) MD simulation profiles of the R148C mutant showing stable temperature and energy equilibration, with increased fluctuations in Rg and RMSD compared to the wild-type protein and (c) MD simulation profiles of the C214Y mutant showing stable temperature and energy profiles, accompanied by greater variations in Rg and RMSD, indicating altered structural dynamics relative to the wild type

Furthermore, the results from energy, RMSD, and Rg analyses consistently indicate that both Arg148Cys and Cys214Tyr mutations destabilize the native structure of PrP. The WT protein maintains structural integrity and energetic stability, whereas the mutants fail to achieve stable convergence within the simulation timeframe. Notably, the C214Y mutation exerts a more pronounced destabilizing effect compared to Arg148Cys, as evidenced by greater structural fluctuations and reduced compactness. The present findings highlight the structural destabilization induced by Arg148Cys and Cys214Tyr mutations; however, further investigations are required to fully elucidate their mechanistic impact on prion protein misfolding and pathogenicity. Extended MD simulations over longer timescales, along with enhanced sampling techniques, could provide deeper insights into rare conformational transitions and intermediate states. Additionally, free energy landscape analysis and residue-level interaction mapping may help identify critical destabilizing interactions introduced by these mutations. From a biological perspective, integrating these computational results with experimental validation, such as circular dichroism spectroscopy, fluorescence-based stability assays, or aggregation studies, would strengthen the interpretation of mutation-induced effects. Furthermore, exploring potential small-molecule stabilizers or chaperone interactions could open avenues for therapeutic intervention aimed at restoring native PrP stability or preventing misfolding-associated disease progression.

Prion diseases are a group of fatal neurodegenerative disorders primarily associated with structural misfolding of the human PrP, encoded by the *PRNP* gene. Although SNPs are more commonly found in non-coding regions, a considerable proportion of functionally important variants occur within the coding sequence of *PRNP*[35]. Due to the strong evolutionary conservation of this gene on chromosome 20p13, even single amino acid substitutions can significantly disrupt protein folding, stability, and function. Nearly 50-60 well-characterized pathogenic missense variants strongly linked to inherited prion diseases were identified. These include CJD, FFI, and GSS, which represent the principal clinical forms of human prion

disorders. Moreover, *PRNP* mutations have been documented across several mammalian species, including scrapie in sheep and goats, BSE in cattle, CWD in cervids, transmissible mink encephalopathy (TME), and feline spongiform encephalopathy (FSE) in felids[36]. Prior experimental and computational evidence consistently shows that these mutations destabilize the native prion protein structure and enhance its conversion to the pathogenic PrP^{Sc} form. Structurally, the PrP consists of a flexible N-terminal region and a predominantly α-helical C-terminal domain that is critical for maintaining native stability[37]. Mutations such as E200K, D178N, and M129V have been widely studied for their structural and clinical effects. E200K is strongly associated with familial CJD, whereas D178N results in distinct disease phenotypes depending on the residue at codon 129. The M129V polymorphism acts as an important modifier of disease susceptibility and clinical variability[4,38].

Moreover, D202N affects α3-helix stability, Q212P alters loop conformation, and T183A compromises domain integrity. These substitutions destabilize the native PrP^{C} structure and increase its tendency to adopt the β-sheet–rich PrP^{Sc} conformation, which aggregates into amyloid fibrils[39]. In addition, variations within the octapeptide repeat region and other conserved motifs affect copper binding, structural stability, and redox balance, thereby influencing disease progression. The primary pathogenic mechanism involves misfolding of PrP^{C} into PrP^{Sc}, which leads to amyloid deposition, spongiform degeneration, astrocytosis, and neuronal loss[40]. In normal physiology, *PRNP* is highly expressed in the central nervous system and is involved in neuroprotection, synaptic function, cell adhesion, and circadian regulation. Its octapeptide repeat region binds copper ions and may influence the activity of Cu-Zn superoxide dismutase (SOD1), thereby contributing to antioxidant defense and cellular homeostasis[41]. Beyond *PRNP* itself, literature reported genome-wide association studies have identified several modifier genes, including MAPT, APOE, BACE1, and STX6, indicating that prion diseases involve complex interactions across multiple neurodegenerative pathways[42].

This study identifies functionally important nsSNPs in the *PRNP* gene and to investigate their structural and dynamic impacts using an integrated computational approach. Variant data were retrieved from publicly available databases, followed by systematic screening using multiple sequence and structure-based prediction tools to detect deleterious and disease-associated substitutions. Variants consistently classified as damaging were subsequently evaluated for their effects on protein stability using consensus-based methods. Three-dimensional structures of both wild-type and mutant prion proteins were constructed through homology and ab initio modeling, followed by refinement and validation to ensure structural accuracy. In addition, molecular docking was conducted to examine ligand-binding affinity and interaction profiles within predicted active sites. Protein flexibility and dynamic stability were further evaluated through normal mode analysis and molecular dynamics simulations under physiological conditions, using parameters such as RMSD, potential energy, and radius of gyration.

Using this workflow, a subset of nsSNPs with potential functional relevance was prioritized from a large dataset, consistent with the expected low proportion of coding variants in the human genome. Multi-tool screening identified several consistently deleterious substitutions, including Gly127Val, Cys214Tyr, Pro50Leu, Pro76Arg, Pro102Leu, Pro105Leu, Gly131Val, His187Arg, Arg148Cys, Gly29Glu, and Gly58Trp. The convergence of independent prediction methods supports the likelihood that these variants may significantly disrupt prion protein structure and function, justifying their selection for downstream structural and dynamic analyses. Disease association analysis further reinforced the pathogenic significance of key variants, particularly Gly127Val, Cys214Tyr, Gly131Val, Arg148Cys, and Gly58Trp, which were consistently classified as disease-causing across predictive platforms. Stability assessment revealed that the majority of nsSNPs, including Cys214Tyr and Arg148Cys, are associated with reduced protein stability, indicating that structural destabilization is a common mechanism underlying prion protein dysfunction.

For structural analysis, the Cys214Tyr substitution replaces a small and structurally important cysteine residue with a bulkier tyrosine, which is expected to disturb local packing and weaken hydrophobic interactions within the protein core. Literature reported evidence shows that Cys214 is involved in the conserved Cys179-Cys214 disulfide bond, a key structural element required for maintaining the native α-helical stability of the prion protein. Disruption in this region has been associated with reduced structural integrity and increased local flexibility of PrP^{43}. In contrast, the Arg148Cys substitution results in the loss of a positively charged arginine residue and its replacement with a neutral cysteine. This change may weaken electrostatic interactions and disturb surface charge distribution that contributes to protein-protein interaction stability. Literature reports indicate that alterations in charged residues of PrP can destabilize native interaction networks and modify conformational behavior. Comparative modeling and validation identified a high-quality structural model suitable for downstream analyses. The selected model exhibited strong stereochemical properties and a predominantly α-helical architecture, consistent with the known structure of the prion protein. Structural features, including flexible loop regions and moderate solvent accessibility, suggest that certain regions of the protein are more susceptible to conformational perturbation. These characteristics may facilitate the transition from the native form to aggregation-prone conformations.

Furthermore, Binding site analysis identified three potential ligand-binding pockets located in regions associated with structural stability and functional regulation of the prion protein. A library of 20 compounds, comprising approved drugs, withdrawn molecules, and experimentally reported anti-prion and anti-aggregation agents, was evaluated for their potential to inhibit PrP misfolding and aggregation. ADMET and drug-likeness profiling using SwissADME revealed considerable variability in pharmacokinetic behavior among the selected compounds. Most compounds exhibited limited oral bioavailability due to high molecular weight, elevated polar surface area, and structural complexity. Only a small subset satisfied lead-likeness criteria, with trehalose and flupirtine showing comparatively favorable drug-likeness and synthetic accessibility profiles. In addition, several compounds showed liabilities such as P-glycoprotein efflux susceptibility and CYP450 inhibition, indicating potential limitations for central nervous system delivery and an increased risk of drug-drug interactions.Our molecular docking results demonstrated that 14 compounds retained strong binding affinity toward the prion protein. Namely, astemizole, flunarizine, simvastatin, rifampicin, tacrolimus, and amphotericin B consistently showed favorable binding energies across both wild-type and mutant structures. Although the Cys214Tyr and Arg148Cys mutations generally reduced binding affinity, several ligands maintained stable interactions, suggesting that key binding pockets retain partial structural integrity despite mutation-induced perturbations. Interaction analysis further indicated that ligand binding is primarily stabilized through hydrogen bonding, hydrophobic interactions, and π-mediated contacts within functionally important regions of PrP. The most frequently identified residues across docking, FT-Site prediction, and literature reports included ARG136, MET134, GLN212, GLU207, ARG208, MET213, VAL161, VAL176, VAL180, and CYS214, all of which consistently participated in ligand interactions. These residues are known to play essential roles in maintaining prion protein structural stability and functional integrity. In particular, His187, Lys185, Arg208, and Met213 have been previously reported in literature as key contributors to PrP stability and molecular recognition processes. The consistent involvement of these residues across all analyses confirms that the predicted binding pockets are biologically relevant and represent potential therapeutic targets.

The identified compounds that maintained stable binding across mutant prion protein forms represent promising scaffolds for the development of anti-prion therapeutics. However, limitations in pharmacokinetic properties, particularly poor CNS penetration and metabolic instability, highlight the need for structural optimization to enhance therapeutic efficacy and minimize off-target effects. Docking-based studies have been widely employed to characterize ligand-PrP interactions, estimate binding affinities, and identify druggable sites. Despite encouraging preclinical outcomes, several compounds,

including phenothiazine and polythiophene derivatives, have failed to demonstrate clinical efficacy. This has been attributed to their preferential binding to the native PrP^{C} rather than the PrP^{SC}, underscoring the importance of targeting disease-relevant structural states. Natural polyphenolic compounds have gained attention due to their dual role in inhibiting amyloid aggregation and mitigating oxidative stress. These molecules interfere with fibril nucleation and elongation while reducing cellular damage caused by reactive oxygen and nitrogen species. Experimental evidence indicates that quercetin enhances the clearance of prion aggregates and alleviates oxidative stress, supporting its therapeutic potential in prion-associated neurodegeneration.

Normal mode analysis revealed that the Arg148Cys and Cys214Tyr mutations significantly alter prion protein dynamics. Increased eigenvalues relative to the wild-type indicate reduced flexibility and enhanced structural rigidity in the mutants. These effects are accompanied by localized fluctuations in deformability and B-factor profiles, particularly in loop regions critical for conformational transitions. The MD simulations further corroborated these findings. The wild-type protein exhibited stable energy convergence, compactness, and consistent RMSD profiles, reflecting structural integrity. In contrast, mutant proteins displayed persistent fluctuations in potential energy, RMSD, and radius of gyration, indicating reduced stability and partial unfolding. Among them, Cys214Tyr exerted a more pronounced destabilizing effect, suggesting greater disruption of protein folding. Consistent with previous studies, prion-associated mutations destabilize the C-terminal α-helical domain, leading to increased flexibility, disruption of hydrogen bonding networks, loss of salt bridges, and enhanced backbone mobility. These structural perturbations facilitate protein misfolding and promote conversion to the pathogenic PrP^{SC} form.

The primary novelty of this study lies in the implementation of a comprehensive, multi-layered computational pipeline for systematic analysis of *PRNP* variants. This integrated framework combines nsSNP prioritization, stability prediction, structural modeling, molecular docking, normal mode analysis, and molecular dynamics simulations. Such an approach provides a more complete understanding of how genetic variations influence prion protein structure, dynamics, and ligand interactions. Additionally, the simultaneous evaluation of both previously reported pathogenic mutations and newly predicted variants enhances the robustness and biological relevance of the findings. The integration of structural stability assessment with ligand-binding analysis offers a holistic perspective on prion dysfunction and therapeutic targeting. Despite these strengths, several limitations must be acknowledged. Computational predictions rely on theoretical models that cannot fully capture the complexity of biological systems. Molecular docking and dynamics simulations were conducted under simplified conditions, which may not accurately represent physiological environments, membrane interactions, or long-timescale aggregation processes. Structural modeling is also dependent on available templates, and although validation metrics indicated high-quality models, minor deviations from experimental structures may persist.

Furthermore, ligand screening was restricted to a predefined compound library, potentially limiting chemical diversity and the identification of more potent candidates. Future studies should focus on improving predictive accuracy through advanced sampling techniques and extended molecular dynamics simulations to better capture rare conformational transitions involved in prion misfolding. Incorporating free energy calculations and ensemble docking strategies may further refine ligand selection and binding stability assessment across multiple conformational states. Experimental validation is essential to substantiate computational findings, techniques such as circular dichroism spectroscopy, Thioflavin T assays, fluorescence-based stability measurements, and cell-based prion propagation models will be critical for verifying structural and functional outcomes. *In vivo* studies are also necessary to evaluate pharmacokinetics, blood–brain barrier permeability, toxicity, and therapeutic efficacy. From a therapeutic perspective, future efforts should prioritize structure-guided optimization of lead compounds to enhance CNS delivery and reduce off-target interactions. Targeting early misfolding intermediates of PrP, rather than fully aggregated PrP^{Sc} species, may offer a more effective strategy for intervention.

CONCLUSION

This study presents a comprehensive *in silico* investigation of nsSNPs in the *PRNP* gene, integrating sequence-based prediction, structural modeling, molecular docking, normal mode analysis, and molecular dynamics simulations to elucidate their functional and structural consequences. From an extensive variant dataset, a subset of deleterious mutations, including Gly127Val, Cys214Tyr, Gly131Val, Arg148Cys, and Gly58Trp, was prioritized based on consistent predictions across multiple computational platforms, reinforcing their potential role in prion protein dysfunction. Structural and stability analyses demonstrated that most identified nsSNPs contribute to reduced protein stability, with Cys214Tyr and Arg148Cys showing pronounced destabilizing effects. These substitutions disrupt key structural features, including disulfide bonding, electrostatic interactions, and local packing, thereby increasing conformational flexibility and favoring misfolding-prone states. Virtual screening and docking analyses identified several compounds with strong binding affinity toward both native and mutant prion protein forms, including astemizole, flunarizine, simvastatin, rifampicin, tacrolimus, and amphotericin B. Despite mutation-induced reductions in binding affinity, several ligands maintained stable interaction profiles, suggesting partial preservation of druggable binding pockets. Interaction mapping revealed that residues such as ARG136, MET134, GLN212, GLU207, ARG208, MET213, VAL161, VAL176, VAL180, and CYS214 consistently participate in ligand recognition and are critical for maintaining the structural integrity and functional stability of PrP. The MD simulations further confirmed that these variants compromise the thermodynamic stability of the prion protein, as evidenced by increased fluctuations in RMSD, radius of gyration, and potential energy compared to the wild-type structure. Overall, the findings indicate that *PRNP* nsSNPs significantly influence prion protein stability, dynamics, and ligand interaction behavior. The integration of genetic, structural, and pharmacological analyses provides a robust framework for identifying high-risk variants and prioritizing potential therapeutic candidates. This work contributes to a deeper mechanistic understanding of mutation-driven prion misfolding and offers a valuable foundation for structure-guided anti-prion drug development.

SIGNIFICANCE STATEMENT

This study provides a comprehensive computational evaluation of pathogenic *PRNP* mutations and their structural consequences using integrated bioinformatics, molecular docking, and molecular dynamics simulations. The findings identify critical mutations that destabilize the prion protein and highlight promising compounds with potential to stabilize its native structure. These results enhance the understanding of mutation-driven prion protein dysfunction and offer a valuable foundation for future experimental validation and the development of targeted therapeutic strategies against prion diseases.

ACKNOWLEDGMENT

We appreciate the contributions of all who contributed to this study work.

REFERENCES

1. Abuzaid, O., A.B. Idris, S. Yılmaz, E.B. Idris, L.B. Idris and M.A. Hassan, 2024. Prediction of the most deleterious non-synonymous SNPs in the human *IL1B* gene: Evidence from bioinformatics analyses. BMC Genomic Data, Vol. 25. 10.1186/s12863-024-01233-x.
2. Zhao, J., S. Zhang, Y. Jiang, Y. Liu and Q. Zhu, 2023. Mutation analysis of pathogenic non-synonymous single nucleotide polymorphisms (nsSNPs) in WFS1 gene through computational approaches. Sci. Rep., Vol. 13. 10.1038/s41598-023-33764-1.
3. Corbie, R., T. Campbell, L. Darwent, P. Rudge, J. Collinge and S. Mead, 2022. Estimation of the number of inherited prion disease mutation carriers in the UK. Eur. J. Hum. Genet., 30: 1167-1170.
4. Bernardi, L. and A.C. Bruni, 2019. Mutations in prion protein gene: Pathogenic mechanisms in C-terminal vs. N-terminal domain, a review. Int. J. Mol. Sci., Vol. 20. 10.3390/ijms20143606.
5. Tan, T.H.L., R.J. Stark, J.A. Waterston, O. White, D. Thyagarajan and M. Monif, 2020. Genetic prion disease: D178N with 129MV disease modifying polymorphism-a clinical phenotype. BMJ Neurol. Open, Vol. 2. 10.1136/bmjno-2020-000074.

6. Appleby, B.S., M. Manca, M.S. Piazza, T.D. Kerr and A. Cornacchia *et al*., 2026. Genetic Creutzfeldt-Jakob disease linked to the E200K mutation: A large cohort study. Acta Neuropathol., Vol. 151. 10.1007/s00401-026-02975-x.
7. Kim, Y.C. and B.H. Jeong, 2021. The first meta-analysis of the M129V single-nucleotide polymorphism (SNP) of the prion protein gene (*PRNP*) with sporadic Creutzfeldt-Jakob disease. Cells, Vol. 10. 10.3390/cells10113132.
8. Benavente, R. and R. Morales, 2024. Therapeutic perspectives for prion diseases in humans and animals. PLoS Pathog., Vol. 20. 10.1371/journal.ppat.1012676.
9. Bagyinszky, E., V. van Giau, Y.C. Youn, S.S.A. An and S. Kim, 2018. Characterization of mutations in *PRNP* (prion) gene and their possible roles in neurodegenerative diseases. Neuropsychiatr. Dis. Treat., 2018: 2067-2085.
10. Alsiary, R.A., M. Alghrably, A. Saoudi, S. Al-Ghamdi, L. Jaremko, M. Jaremko and A.H. Emwas, 2020. Using NMR spectroscopy to investigate the role played by copper in prion diseases. Neurol. Sci., 41: 2389-2406.
11. Kovacs, G.G. and H. Budka, 2009. Molecular pathology of human prion diseases. Int. J. Mol. Sci., 10: 976-999.
12. Castle, A.R. and A.C. Gill, 2017. Physiological functions of the cellular prion protein. Front. Mol. Biosci., Vol. 4. 10.3389/fmolb.2017.00019.
13. Nafe, R., C.T. Arendt and E. Hattingen, 2023. Human prion diseases and the prion protein-what is the current state of knowledge? Transl. Neurosci., Vol. 14. 10.1515/tnsci-2022-0315.
14. Appleby, B.S., S. Shetty and M. Elkasaby, 2022. Genetic aspects of human prion diseases. Front. Neurol., Vol. 13. 10.3389/fneur.2022.1003056.
15. Sardar, N., A. Noman, K. Ramzan, I. Bilal and A. Islam *et al*., 2025. Exploring the impact of STAT4 non-synonymous mutations on hepatitis B virus susceptibility: A bioinformatics approach. Int. J. Mol. Microbiol., 8: 79-102.
16. Tariq, H., M. Asif, M. Saleem, K. Ramzan, M. Zulfiqar, A. Amira and A.R. Asif, 2024. Evaluation of detrimental missense SNPs of human *CXCL6* gene by combining algorithms, homology modeling, and molecular docking. Int. J. Biol. Res., 4: 92-106.
17. de Oliveira Garcia, F.A., E.S. de Andrade and E.I. Palmero, 2022. Insights on variant analysis *in silico* tools for pathogenicity prediction. Front. Genet., Vol. 13. 10.3389/fgene.2022.1010327.
18. Akter, S., M. Fuad, Z. Mahmud, S. Tamanna, M. Sayem, K.H. Raj and M.Z.H. Howlader, 2025. Comprehensive *in silico* characterization of nonsynonymous SNPs in the human ezrin (EZR) gene and their role in disease pathogenesis. Biochem. Biophys. Rep., Vol. 42. 10.1016/j.bbrep.2025.101972.
19. Waheed, S., K. Ramzan, S. Ahmad, M.S. Khan and M. Wajid *et al*., 2024. Identification and *in-silico* study of non-synonymous functional SNPs in the human *SCN9A* gene. PLoS ONE, Vol. 19. 10.1371/journal.pone.0297367.
20. Noman, A., N. Sardar, A. Islam, K. Ramzan and M.Z. Ali *et al*., 2025. Integrative computational analysis of CFTR mutations linked to cystic fibrosis. Int. J. Mol. Microbiol., 8: 52-69.
21. Ahmed, E.M., M.E. Elangeeb, K.M. Adam, H.A. Abuagla and A.A.E.M. Ahmed *et al*., 2024. Computational analysis of deleterious nsSNPs in *INS* gene associated with permanent neonatal diabetes mellitus. J. Pers. Med., Vol. 14. 10.3390/jpm14040425.
22. Tariq, H., M. Saleem, A.H. Ali, M. Fatima and A. Fatima *et al*., 2026. Integrative computational approaches to protein structure and drug design in POEMS syndrome. Int. J. Mol. Microbiol., 9: 17-35.
23. Ramzan, K., S. Sabri, D.S. Alshaya, S. Ramzan and M.S. Khan *et al*., 2024. Homology modeling and structural docking analysis on a human *BDNF* gene by using computational algorithms. Res. Square, 10.21203/rs.3.rs-5294979/v1.
24. Khalid, Z. and O. Almaghrabi, 2020. Mutational analysis on predicting the impact of high-risk SNPs in human secretary phospholipase A2 receptor (PLA2R1). Sci. Rep., Vol. 10. 10.1038/s41598-020-68696-7.
25. Younus, S., Ö. Tatli, A. Nasimian, J.U. Kazi and L. Rönnstrand, 2025. Understanding the characteristic behaviour of the wild-type and mutant structure of FLT3 protein by computational methods. Comput. Struct. Biotechnol. J., 27: 4526-4542.

26. Khan, M.U., A. Sakhawat, R. Rehman, A.H. Wali and M.U. Ghani *et al*., 2024. Identification of novel natural compounds against CFTR p.Gly628Arg pathogenic variant. AMB Express, Vol. 14. 10.1186/s13568-024-01762-9.
27. Kozakov, D., L.E. Grove, D.R. Hall, T. Bohnuud and S.E. Mottarella *et al*., 2015. The FTMap family of web servers for determining and characterizing ligand-binding hot spots of proteins. Nat. Protoc., 10: 733-755.
28. Kochnev, Y., E. Hellemann, K.C. Cassidy and J.D. Durrant, 2020. Webina: An open-source library and web app that runs AutoDock Vina entirely in the web browser. Bioinformatics, 36: 4513-4515.
29. Uzoeto, H.O., S. Cosmas, J.N. Ajima, A.V. Arazu and C.M. Didiugwu *et al*., 2022. Computer-aided molecular modeling and structural analysis of the human centromere protein-HIKM complex. Beni-Suef Univ. J. Basic Appl. Sci., Vol. 11. 10.1186/s43088-022-00285-1.
30. Khatoon, M., Y.S. Sekar, S. Rani, V. Ramesh and M. Shijili *et al*., 2025. Computational analysis of non-synonymous SNP effects on human PLVAP gene structure and function. J. Appl. Genet., 10.1007/s13353-025-01038-3.
31. Ślusarz, R., A.K. Sieradzan, A. Giełdoń, E.A. Lubecka and M.J. Ślusarz *et al*., 2025. UNRES web server: Extensions to nucleic acids, prediction of peptide aggregation, and new types of restrained calculations. J. Mol. Biol., Vol. 437. 10.1016/j.jmb.2025.168968.
32. Biasini, E., L. Tapella, E. Restelli, M. Pozzoli, T. Massignan and R. Chiesa, 2010. The hydrophobic core region governs mutant prion protein aggregation and intracellular retention. Biochem. J., 430: 477-486.
33. Chen, J. and D. Thirumalai, 2013. Helices 2 and 3 are the initiation sites in the $PrP^{C}\rightarrow PrP^{SC}$ transition. Biochemistry, 52: 310-319.
34. van der Kamp, M.W. and V. Daggett, 2010. Pathogenic mutations in the hydrophobic core of the human prion protein can promote structural instability and misfolding. J. Mol. Biol., 404: 732-748.
35. Han, C.S., S.Y. Won, S.H. Park, Y.C. Kim, 2025. Identification of the highly polymorphic prion protein gene (*PRNP*) in frogs (*Rana dybowskii*). Animals, Vol. 15. 10.3390/ani15020220.
36. Imran, M. and S. Mahmood, 2011. An overview of animal prion diseases. Virol. J., Vol. 20. 10.1186/1743-422X-8-493.
37. Requena, J.R. and H. Wille, 2014. The structure of the infectious prion protein: Experimental data and molecular models. Prion, 8: 60-66.
38. Mead, S., S. Lloyd and J. Collinge, 2019. Genetic factors in mammalian prion diseases. Annu. Rev. Genet., 53: 117-147.
39. D'Angelo, P., S.D. Longa, A. Arcovito, G. Mancini and A. Zitolo *et al*., 2012. Effects of the pathological Q212P mutation on human prion protein non-octarepeat copper-binding site. Biochemistry, 51: 6068-6079.
40. Thody, S.A., M.K. Mathew and J.B. Udgaonkar, 2018. Mechanism of aggregation and membrane interactions of mammalian prion protein. Biochim. Biophys. Acta, Biomembr., 1860: 1927-1935.
41. Linden, R., 2017. The biological function of the prion protein: A cell surface scaffold of signaling modules. Front. Mol. Neurosci., Vol. 10. 10.3389/fnmol.2017.00077.
42. Mead, S., J. Uphill, J. Beck, M. Poulter and T. Campbell *et al*., 2012. Genome-wide association study in multiple human prion diseases suggests genetic risk factors additional to PRNP. Hum. Mol. Genet., 21: 1897-1906.
43. Ning, L., J. Guo, N. Jin, H. Liu and X. Yao, 2014. The role of Cys179-Cys214 disulfide bond in the stability and folding of prion protein: Insights from molecular dynamics simulations. J. Mol. Model., Vol. 20. 10.1007/s00894-014-2106-y.

SUPPLEMENTARY DATA

Table S1: Comprehensive URL links for PrP bioinformatics workflow

Tool/Software	URL	Role in study
NCBI dbSNP	https://www.ncbi.nlm.nih.gov/snp/	Retrieval of PrP variants and SNP data
UniProt	https://www.uniprot.org	Protein sequence retrieval (PrP, P04156)
SNPNexus v4	https://www.snp-nexus.org/v4/	Prediction of deleterious nsSNPs based on sequence conservation
PolyPhen-2	http://genetics.bwh.harvard.edu/pph2/	Functional impact prediction of amino acid substitutions
PROVEAN	http://provean.jcvi.org/	Assessment of functional effect of mutations
SNap	https://statgen.uni-koeln.de/software/snap2/design.html	Machine-learning-based variant effect prediction
CADD	https://cadd.gs.washington.edu/	Integrated deleteriousness scoring of variants
ConDEL	https://bbglab.irbbarcelona.org/fannsdb/	Consensus deleteriousness prediction
Align-GVGD	http://agvgd.hci.utah.edu/	Classification of missense variant impact
PredictSNP	https://loschmidt.chemi.muni.cz/predictsnp1/	Consensus disease prediction of SNPs
P-Mut	https://bio.tools/pmut	Disease association prediction
PhD-SNP	https://snps.biofold.org/phd-snp/phd-snp.html	Classification of disease-related mutations
SNPs&GO	https://snps-and-go.biocomp.unibo.it/snps-and-go	GO-based disease prediction of SNPs
Meta-SNP	https://snps.biofold.org/meta-snp	Meta-predictor for disease association
SuSPect	http://www.sbg.bio.ic.ac.uk/suspect	Functional impact prediction using protein networks
I-Mutant 2.0	https://folding.biofold.org/i-mutant/i-mutant2.0.html	Protein stability change prediction
MUpro	http://mupro.proteomics.ics.uci.edu	Stability effect prediction using machine learning
iStable 2.0	http://predictor.nchu.edu.tw/iStable	Integrated protein stability prediction
HOPE Project	https://www3.cmbi.umcn.nl/hope/input/	Structural effects of selected nsSNPs
MODELLER v10.5	https://salilab.org/modeller/10.5/release.html	Homology modeling of protein structures
SWISS-MODEL	https://swissmodel.expasy.org/	Template-based protein structure modeling
i-TASSER	https://zhanggroup.org/I-TASSER/	Ab initio and threading-based structure prediction
trRosetta	https://yanglab.qd.sdu.edu.cn/trRosetta/	Deep learning-based protein structure prediction
ModRefiner	https://zhanggroup.org/ModRefiner/	Structural refinement of protein models
SAVES v6.1 Server	https://saves.mbi.ucla.edu/	Structural validation (PROCHECK, ERRAT, Verify3D)
TM-align	https://zhanggroup.org/TM-align/	Structural alignment and RMSD calculation
PyMOL	https://pymol.org/2/	Visualization and mutation modeling
PubChem	https://pubchem.ncbi.nlm.nih.gov/	Retrieval of ligand structures
AutoDock Tools	http://autodock.scripps.edu/	Preparation of docking files (PDBQT conversion)
Active site prediction server	https://scfbio-iitd.res.in/dock/ActiveSite.jsp	Prediction of ligand-binding sites
Webina 1.0.5	https://durrantlab.pitt.edu/webina/	Molecular docking simulations
Discovery studio visualizer	https://discover.3ds.com/discovery-studio-visualizer	Protein–ligand interaction analysis
iMODS	http://imods.chaconlab.org/	Normal mode analysis of protein flexibility
UNRES Server	https://unres-server.chem.ug.edu.pl	Molecular dynamics simulations

Table S2: *In silico* functional prediction of deleterious nsSNPs in the studied gene using multiple bioinformatics tools

SNVs	Protein change	Variant consequence	SIFT		Polyphen		Ph-2		PROVEAN		CADD	SNaP		CONDEL		Predict SNP	A-AVGD	
			E	Sc	E	Sc	E	Sc	E	Sc	Sc	E	Sc	E	Score	E	C	E
rs267606980	Gly127Val	Missense	D	0	PD	1	PD	1	D	-3.44	26.1	E	81	D	0.59417432	D	Class C65	D
rs915073935	Arg136Trp	Missense	D	0.02	PD	1	PD	1	N	-1.463	25.1	E	71	D	0.599108654	D	Class C65	D
rs150351644	Gly142Cys	Missense	D	0.01	PD	1	PD	1	N	-1.822	25.8	E	42	D	0.592961693	D	Class C65	D
rs374528688	Gly195Arg	Missense	D	0.02	PD	1	PD	1	N	-1.968	28.8	E	34	D	0.601820706	D	Class C65	D
rs761807915	Asp202Asn	Missense	D	0.04	PD	1	PD	1	N	-1.198	27	E	60	D	0.595983354	D	Class C15	LessLikely
rs1180897417	Cys214Tyr	Missense	D	0	PD	1	PD	1	D	-3.765	26.4	E	73	D	0.665505987	D	Class C65	D
rs775737462	Ser236Phe	Missense	D	0	PD	1	PD	1	N	-1.68	25.9	E	45	D	0.580051523	D	Class C65	D
rs771239157	Phe12Ser	Missense	D	0	PD	0.999	PD	0.999	N	-0.734	28.5	E	81	D	0.560696014	D	Class C65	D
rs1197612803	Lys24Arg	Missense	D	0.02	PD	0.999	PD	0.998	N	-1.033	26.5	E	26	D	0.57790256	D	Class C25	LessLikely
rs758452370	Gly35Ala	Missense	D	0.01	PD	0.999	PD	1	N	-2.475	25.3	E	19	D	0.55136859	D	Class C55	D
rs1379757697	Pro50Leu	Missense	D	0	PD	0.999	PD	1	D	-3.483	25.7	E	62	D	0.544524512	D	Class C65	D
rs778667313	Pro76Arg	Missense	D	0.02	PD	0.999	PD	1	D	-3.915	24.1	E	50	D	0.583972651	D	Class C65	D
rs1279036396	Gly92Glu	Missense	D	0.03	PD	0.999	PD	1	N	-1.253	23.4	E	32	D	0.543385182	D	Class C65	D
rs74315401	Pro102Leu	Missense	D	0	PD	0.999	PD	1	D	-3.392	25.6	E	84	D	0.585354452	D	Class C65	D
rs11538758	Pro105Leu	Missense	D	0	PD	0.999	PD	1	D	-3.271	25.4	E	84	D	0.589709258	D	Class C65	D
rs11538769	Gly114Ser	Missense	D	0.01	PD	0.999	PD	1	N	-1.21	27.7	E	50	D	0.566387587	D	Class C55	D
rs752571244	Val122Gly	Missense	D	0.03	PD	0.999	PD	1	N	-0.217	24.6	N	-18	D	0.536718489	N	Class C65	D
rs74315410	Gly131Val	Missense	D	0	PD	0.999	PD	1	D	-2.879	26	E	84	D	0.569652944	D	Class C65	D
rs1323478206	Arg156His	Missense	D	0	PD	0.999	PD	1	N	-1.737	26.4	E	74	D	0.611873036	D	Class C25	D
rs74315403	Asp178Asn	Missense	D	0	PD	0.999	PD	1	N	-1.531	28.5	E	94	D	0.61247114	D	Class C15	LessLikely
rs74315413	His187Arg	Missense	D	0.01	PD	0.999	PD	1	D	-2.607	25.6	E	87	D	0.596415963	D	Class C25	D
rs1489076172	Pro238Leu	Missense	D	0.01	PD	0.999	PD	1	N	-1.551	24.9.	E	57	D	0.584923778	D	Class C65	D

Table S2: Continue

SNVs	Protein change	Variant consequence	SIFT		Polyphen		Ph-2		PROVEAN		CADD	SNaP		CONDEL		Predict SNP	A-AVGD	
			E	Sc	E	Sc	E	Sc	E	Sc	Sc	E	Sc	E	Score	E	C	E
rs1412795882	Leu250Pro	Missense	D	0	PD	0.999	PD	0.999	N	-0.591	28.7	E	70	D	0.541357305	D	Class C65	D
rs74315414	Pro105Thr	Missense	D	0.01	PD	0.998	PD	1	N	-2.333	24.3	E	84	D	0.589258521	D	Class C35	D
rs74315411	Thr183Ala	Missense	D	0	PD	0.998	PD	0.999	N	-1.785	25	E	71	D	0.605325331	D	Class C55	D
rs28933385	Glu200Lys	Missense	D	0	PD	0.998	PD	1	N	-1.478	39	E	88	D	0.614025552	D	Class C55	D
rs769904669	Ser236Thr	Missense	D	0.02	PD	0.998	PD	0.999	N	-0.779	27.2	N	-11	D	0.580611659	D	Class C55	D
rs1313855686	Arg37Gln	Missense	D	0	PD	0.997	PD	1	N	-0.853	28.4	E	62	D	0.545894121	D	Class C35	D
rs748501151	Asn153Ser	Missense	D	0.01	PD	0.996	PD	1	N	-1.337	26.7	E	23	D	0.609925429	D	Class C45	D
rs1245225352	Tyr157His	Missense	D	0	PD	0.995	PD	1	N	-1.697	25.4	E	80	D	0.610919321	D	Class C65	D
rs1299768716	Tyr150His	Missense	D	0	PD	0.992	PD	1	N	-1.498	28.1	E	80	D	0.604144855	D	Class C65	D
rs921542806	Tyr163His	Missense	D	0.02	PD	0.987	PD	1	N	-1.277	24.9	E	82	D	0.614217885	D	Class C65	D
rs751211144	Arg25Cys	Missense	D	0	PD	0.982	PD	1	N	-1.8	26.1	E	65	D	0.559340574	D	Class C65	D
rs146939732	Arg25His	Missense	D	0.02	PD	0.982	PD	0.999	N	-1.317	26.7	E	36	D	0.55867685	D	Class C25	D
rs750548556	Arg148Cys	Missense	D	0	PD	0.98	PD	1	D	-3.202	28.8	E	40	D	0.61355102	D	Class C65	D
rs11538755	Pro26Thr	Missense	D	0	PD	0.976	PD	0.996	N	-2.147	23.9	E	51	D	0.546021963	D	Class C35	D
rs372878791	Thr188Met	Missense	D	0.01	PD	0.971	PD	0.999	N	-1.126	24.5	N	-15	D	0.591095781	D	Class C65	D
rs989264799	Gly29Glu	Missense	D	0	PD	1	PD	1	D	-2.566	26.2	E	63	D	0.567334253	D	Class C65	D
rs773938628	Gly58Trp	Missense	D	0.03	PD	1	PD	1	D	-4.133	27.4	E	54	D	0.565637641	D	Class C65	D
rs780369285	Gly127Ser	Missense	D	0	PD	1	PD	1	N	-1.92	27.4	E	76	D	0.59355395	D	Class C55	D
rs1210376979	Lys204Thr	Missense	D	0	PD	0.947	PD	0.991	N	-2.079	27.6	E	38	D	0.562176034	D	Class C65	D
rs748577950	Gly131Arg	Missense	D	0	PD	0.913	PD	0.996	N	-2.451	41	E	89	D	0.569733605	D	Class C65	D
rs751882709	Gln212Pro	Missense	D	0	PD	0.911	PD	0.999	N	-1.585	26.5	E	81	D	0.589250608	D	Class C65	D

*C: Class, D: Deleterious, E: Effect, N: Neutral, PD: Probably damaging and Sc: Score

Table S3: Consensus prediction of disease linked nsSNPs in the *PRNP* gene across multiple *in silico* tools

			SuSPect	SNP and GO	PhD-SNP		Meta-SNP	
SNVs	Protein change	Variant consequence	Effect	Effect	Effect	Score	Effect	Score
rs267606980	Gly127Val	Missense	Disease	Disease	Disease	7	Disease	2
rs915073935	Arg136Trp	Missense	Disease	Disease	Disease	7	Disease	4
rs150351644	Gly142Cys	Missense	Disease	Disease	Disease	6	Disease	3
rs374528688	Gly195Arg	Missense	Neutral	Disease	Disease	2	Neutral	5
rs761807915	Asp202Asn	Missense	Disease	Disease	Disease	5	Disease	2
rs1180897417	Cys214Tyr	Missense	Disease	Disease	Disease	4	Disease	5
rs775737462	Ser236Phe	Missense	Disease	Disease	Disease	3	Disease	3
rs771239157	Phe12Ser	Missense	Disease	Disease	Disease	3	Disease	4
rs1197612803	Lys24Arg	Missense	Neutral	Disease	Neutral	2	Neutral	5
rs758452370	Gly35Ala	Missense	Disease	Disease	Disease	4	Neutral	5
rs1379757697	Pro50Leu	Missense	Disease	Disease	Neutral	5	Neutral	5
rs778667313	Pro76Arg	Missense	Disease	Disease	Neutral	2	Neutral	6
rs1279036396	Gly92Glu	Missense	Neutral	Disease	Disease	5	Disease	2
rs74315401	Pro102Leu	Missense	Disease	Disease	Neutral	3	Neutral	5
rs11538758	Pro105Leu	Missense	Disease	Disease	Neutral	2	Neutral	6
rs11538769	Gly114Ser	Missense	Disease	Disease	Disease	3	Neutral	0
rs752571244	Val122Gly	Missense	Disease	Disease	Neutral	2	Neutral	0
rs74315410	Gly131Val	Missense	Disease	Disease	Disease	8	Disease	3
rs1323478206	Arg156His	Missense	Disease	Disease	Disease	3	Disease	0
rs74315403	Asp178Asn	Missense	Disease	Disease	Disease	4	Disease	4
rs74315413	His187Arg	Missense	Disease	Disease	Disease	5	Neutral	1
rs1489076172	Pro238Leu	Missense	Disease	Disease	Neutral	3	Disease	1
rs1412795882	Leu250Pro	Missense	Disease	Disease	Disease	1	Disease	0
rs74315414	Pro105Thr	Missense	Disease	Disease	Neutral	3	Neutral	6
rs74315411	Thr183Ala	Missense	Disease	Disease	Disease	3	Disease	3
rs28933385	Glu200Lys	Missense	Neutral	Disease	Disease	5	Disease	3
rs769904669	Ser236Thr	Missense	Disease	Disease	Neutral	6	Neutral	5
rs1313855686	Arg37Gln	Missense	Neutral	Disease	Neutral	1	Disease	2
rs748501151	Asn153Ser	Missense	Disease	Disease	Disease	1	Disease	1
rs1245225352	Tyr157His	Missense	Disease	Disease	Disease	2	Disease	1
rs1299768716	Tyr150His	Missense	Disease	Disease	Disease	3	Neutral	0
rs921542806	Tyr163His	Missense	Disease	Disease	Disease	2	Disease	3
rs751211144	Arg25Cys	Missense	Disease	Disease	Disease	6	Disease	2
rs146939732	Arg25His	Missense	Disease	Disease	Disease	3	Disease	2
rs750548556	Arg148Cys	Missense	Disease	Disease	Disease	5	Disease	4
rs11538755	Pro26Thr	Missense	Disease	Disease	Disease	0	Neutral	4
rs372878791	Thr188Met	Missense	Disease	Disease	Disease	2	Neutral	2
rs989264799	Gly29Glu	Missense	Neutral	Disease	Disease	5	Disease	2
rs773938628	Gly58Trp	Missense	Disease	Disease	Disease	8	Disease	3
rs780369285	Gly127Ser	Missense	Disease	Disease	Disease	7	Neutral	1
rs1210376979	Lys204Thr	Missense	Disease	Disease	Disease	4	Neutral	3
rs748577950	Gly131Arg	Missense	Disease	Disease	Disease	8	Disease	4
rs751882709	Gln212Pro	Missense	Disease	Disease	Disease	6	Disease	4

Table S4: Prediction of PrP protein stability changes induced by nsSNPs using computational analysis

			Mu-Pro		I-Mutant		iStable	
SNVs	Protein change	Variant consequence	Prediction	Detal Delta	Stability	RI	Prediction	Score
rs267606980	Gly127Val	Missense	Increase	0.0087191847	Increase	4	Increase	0.517116
rs915073935	Arg136Trp	Missense	Decrease	-0.76259618	Decrease	3	Decrease	0.714629
rs150351644	Gly142Cys	Missense	Decrease	-0.81142928	Decrease	7	Decrease	0.644537
rs374528688	Gly195Arg	Missense	Decrease	-0.41986641	Increase	0	Increase	0.698343
rs761807915	Asp202Asn	Missense	Decrease	-0.77217494	Increase	2	Decrease	0.650823
rs1180897417	Cys214Tyr	Missense	Decrease	-0.89451091	Decrease	0	Decrease	0.820339
rs775737462	Ser236Phe	Missense	Increase	0.097039475	Increase	0	Increase	0.646682
rs771239157	Phe12Ser	Missense	Decrease	-1.9429641	Decrease	8	Decrease	0.778335
rs1197612803	Lys24Arg	Missense	Decrease	-0.40885521	Decrease	1	Decrease	0.737512
rs758452370	Gly35Ala	Missense	Decrease	-0.71310987	Increase	4	Decrease	0.558925
rs1379757697	Pro50Leu	Missense	Decrease	-0.02541924	Increase	2	Increase	0.706906
rs778667313	Pro76Arg	Missense	Decrease	-0.50308396	Increase	4	Decrease	0.527092
rs1279036396	Gly92Glu	Missense	Decrease	-0.01639389	Increase	5	Increase	0.792276
rs74315401	Pro102Leu	Missense	Decrease	-0.015598974	Increase	2	Decrease	0.579282
rs11538758	Pro105Leu	Missense	Decrease	-0.36580668	Increase	5	Decrease	0.619157
rs11538769	Gly114Ser	Missense	Decrease	-0.58962845	Decrease	5	Decrease	0.829575
rs752571244	Val122Gly	Missense	Decrease	-1.7260045	Decrease	9	Decrease	0.887081
rs74315410	Gly131Val	Missense	Increase	0.28170052	Decrease	1	Increase	0.685152
rs1323478206	Arg156His	Missense	Decrease	-1.0619513	Decrease	8	Decrease	0.831248
rs74315403	Asp178Asn	Missense	Decrease	-0.56076231	Decrease	8	Increase	0.731182
rs74315413	His187Arg	Missense	Decrease	-0.48607829	Decrease	6	Increase	0.583045
rs1489076172	Pro238Leu	Missense	Decrease	-0.85915883	Decrease	5	Decrease	0.777169
rs1412795882	Leu250Pro	Missense	Decrease	-2.6293003	Decrease	5	Decrease	0.788417
rs74315414	Pro105Thr	Missense	Decrease	-1.1823593	Decrease	1	Decrease	0.836101
rs74315411	Thr183Ala	Missense	Decrease	-1.5931188	Decrease	9	Decrease	0.792607
rs28933385	Glu200Lys	Missense	Decrease	-1.0813226	Decrease	7	Decrease	0.889049
rs769904669	Ser236Thr	Missense	Decrease	-0.34763322	Decrease	6	Decrease	0.72217
rs1313855686	Arg37Gln	Missense	Decrease	-0.65461065	Decrease	2	Increase	0.521694
rs748501151	Asn153Ser	Missense	Decrease	-1.0581514	Decrease	6	Decrease	0.801832
rs1245225352	Tyr157His	Missense	Decrease	-1.2132105	Decrease	6	Decrease	0.846461
rs1299768716	Tyr150His	Missense	Decrease	-1.137549	Decrease	7	Decrease	0.835129
rs921542806	Tyr163His	Missense	Decrease	-1.2864636	Decrease	6	Decrease	0.842699
rs751211144	Arg25Cys	Missense	Decrease	-0.65200422	Decrease	4	Decrease	0.865441
rs146939732	Arg25His	Missense	Decrease	-0.88784242	Decrease	7	Decrease	0.876943
rs750548556	Arg148Cys	Missense	Decrease	-0.36911104	Decrease	2	Decrease	0.738444
rs11538755	Pro26Thr	Missense	Decrease	-1.6415001	Decrease	5	Decrease	0.851238
rs372878791	Thr188Met	Missense	Decrease	-0.33417365	Decrease	3	Decrease	0.558016
rs989264799	Gly29Glu	Missense	Decrease	-0.05952196	Decrease	1	Decrease	0.72759
rs773938628	Gly58Trp	Missense	Decrease	-0.01667883	Increase	7	Increase	0.772495
rs780369285	Gly127Ser	Missense	Decrease	-0.67756059	Decrease	2	Decrease	0.764821
rs1210376979	Lys204Thr	Missense	Decrease	-0.87259593	Decrease	4	Decrease	0.858281
rs748577950	Gly131Arg	Missense	Decrease	-0.03012247	Decrease	1	Increase	0.717812
rs751882709	Gln212Pro	Missense	Decrease	-1.2016492	Decrease	6	Decrease	0.705803

Table S5: Detailed residue interactions of anti-prion compounds in PrP binding sites

Compound	Protein	Residue(s)	Interaction type
Flunarizine	WT PrP	ARG136	π-Cation/Unfavorable bump
		MET154	π-Sulfur
		GLN212, MET213, CYS214, CYS219, VAL161	Unfavorable bump
		THR216	Halogen (Fluorine)
		ILE215	Alkyl interaction
		SER135, PRO137, ASN159, MET134, GLU211, GLN217, VAL176, VAL180, VAL210, PHE175, TYR163, THR183, GLN160, TYR157, TYR150	van der Waals
Astemizole	WT PrP	TYR162, THR183, TYR218, VAL210, PHE175, PRO158, ASN159, THR216, VAL209, SER135, ILE139, TYR150, TYR157, HIS155	van der Waals
		MET134, CYS179	π-Sulfur
		VAL176	π-Alkyl
		GLN160, VAL164, GLU211, ILE215, GLN212, MET213, GLN180	Unfavorable bump
Simvastatin	WT PrP	ARG136	π-Cation/Unfavorable bump
		PRO158, VAL161, ILE215, GLU211, CYS214	Unfavorable bump
		GLN212	Conventional Hydrogen Bond
		MET134, VAL209	Alkyl interaction
		ASN159, SER135, ILE139, TYR150, ILE138, VAL180, VAL176, PHE175, TYR163, THR183, GLN160, TYR162, CYS179, THR216, GLN217, TYR218	van der Waals
Astemizole	R148C	ARG21, VAL180, TRP162, CYS148, LYS176, GLY214, VAL161, MET213	Unfavorable bump
		ARG21, VAL180, GLN212	Conventional Hydrogen Bond
		VAL209	Halogen (Fluorine)
		MET213	π-Sulfur
		PHE175	π-π Stacked
		ILE139, PHE141	Alkyl interaction
		ILE182, ASP178, HIS177, TYR163, TYR128, ARG164, TYR218, GLN217, GLU207, ASN173, ILE215	van der Waals
Tacrolimus	R148C	HIS140, PHE141, ARG206, GLU176, VAL209, ASN212	Unfavorable bump
		ARG206, GLU176	Unfavorable donor-donor
		GLU207	Conventional Hydrogen Bond
		MET206	Carbon Hydrogen Bond
		VAL180, ILE215	π-Alkyl interaction
		ILE139, PRO137, LEU138, TYR150, TYR157, HIS155, TYR163, CYS179, VAL210, CYS214	van der Waals
Amphotericin B	R148C	SER143, PHE141, HIS140, GLY142, GLN212, ARG208, VAL210, GLU211, ASN214, MET213, ALA161	Unfavorable bump
		ASP148	Conventional Hydrogen Bond
		VAL180, ILE179	π-Alkyl interaction
		ILE138, TYR150, MET205, PRO137, GLN217, THR183, GLY82, HIS177, PHE175, ILE215, GLU146, ASP147	van der Waals
Flunarizine	C214Y	ARG214	π-Cation/Unfavorable bump
		TYR163, VAL209, TYR210, GLN212, CYS179, VAL176, TRP177	Unfavorable bump
		TYR162, VAL161, PHE175, ASN173, ASN174	Halogen (Fluorine)
		VAL180	π-Alkyl
		THR183, MET206, MET213, GLU207, ILE215, GLN217	van der Waals
Rifampicin	C214Y	ARG136	π-π Stacked
		GLU207, ASP178, VAL161	Conventional Hydrogen Bond
		VAL180	π-Alkyl
		TYR162, GLN212, VAL176, VAL209, VAL210, ILE215, PHE141, HIS140	Unfavorable bump
		GLY142, TRP81, ASP147, ILE138, TYR150, PRO137, MET206	van der Waals
Tacrolimus	C214Y	GLN212	Conventional Hydrogen Bond
		ARG208, GLU211	Carbon Hydrogen Bond
		TRP81, VAL180	π-Alkyl
		VAL176, VAL209, ILE139, TYR150, HIS140, PHE141, PRO137	Unfavorable bump
		MET205, MET206, TYR214, HIS127, CYS179, GLY142, SER143, ASP147, ARG151, ILE138, GLU207	van der Waals
		GLU211	Unfavorable donor-donor